Structural and Chemical comparison of brown dwarf protoplanetary disks with T Tauri and Herbig disks

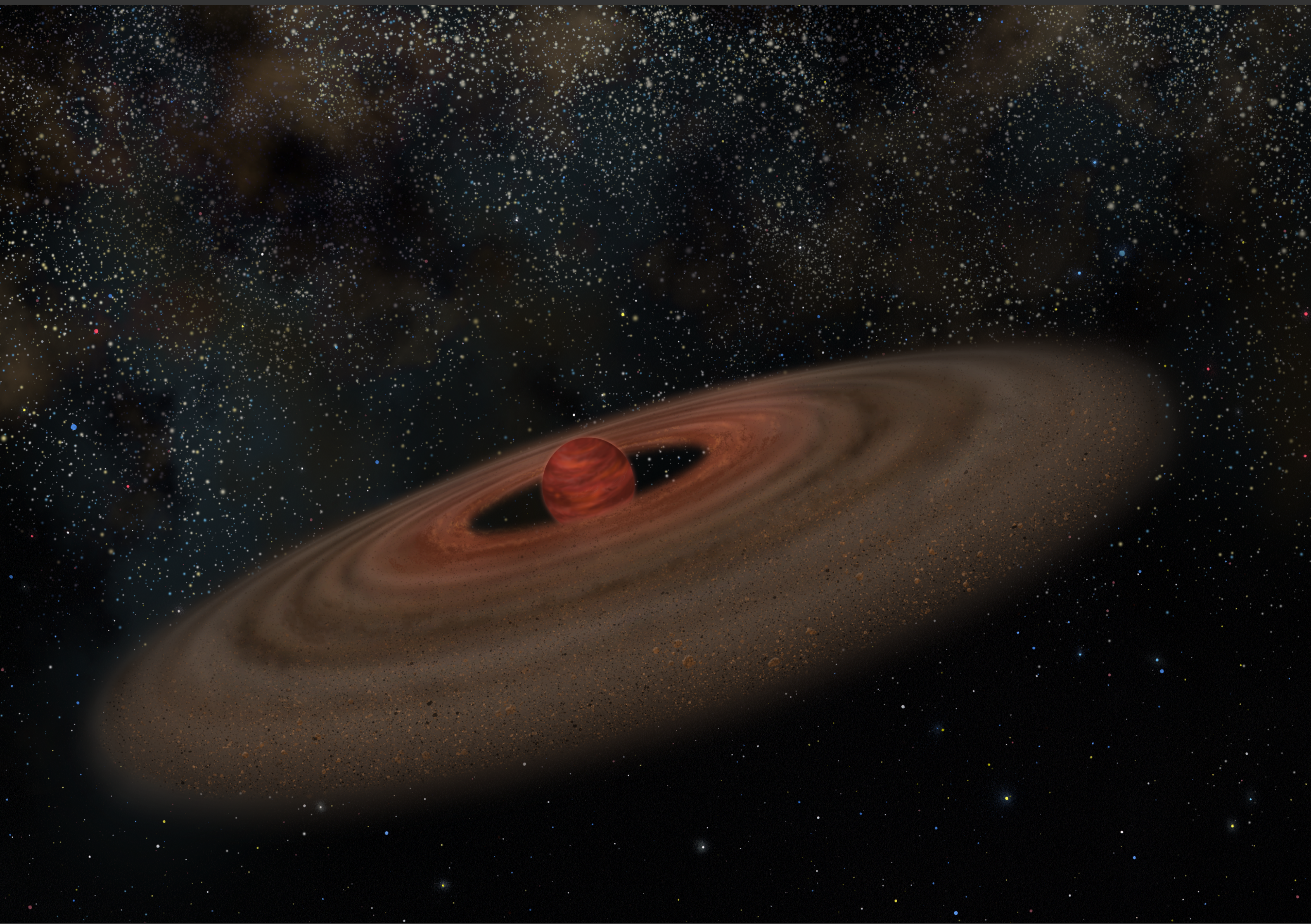

Master Thesis

Balaji Muthusubramanian
Supervisor: Prof. Dr. Inga Kamp

Kapteyn Institute of Astronomy
University of Groningen

Title page image credits:
Gemini Observatory/Association of Universities for Research in Astronomy
http://www.gemini.edu/gallery/v/astronomical_images_and_illustrations/Illustrations/QuadFNL-Edit.jpg.html

ABSTRACT

The formation processes of brown dwarfs is similar to that of low mass stellar counterparts. Hence, the structure of the protoplanetary disk around brown dwarfs could be scaled down versions of that around a low mass T Tauri and Herbig stars. However, each brown dwarf formation path has its impact on the structure of its protoplanetary disk and thus planet formation around them. In our study, we compare the structure and chemistry of a brown dwarf protoplanetary disk with disks around T Tauri and Herbig stars through simple analytic models followed by detailed numerical radiative transfer and thermochemical models using ProDiMo (Woitke et al., 2009). Also a mean Spectral Energy Distribution (SED) compiled from the photometry of 14 brown dwarf protoplanetary disks in the Taurus star forming region was fitted with ProDiMo and the results of the best fitting model was compared with a standard T Tauri ProDiMo model.
The analytic scaling relation predicts the brown dwarf protoplanetary disks to be radially compact ($R_{out} \approx 20 - 40AU$). However, the mean brown dwarf SED predicts extended disks ($R_{out} \approx 200AU$) as one of its possible fitting models. The two different radial structures of the brown dwarf protoplanetary disks can be accounted by their formation scenarios. Processes such as dynamic ejection, photo-erosion by a nearby star, etc. constrains the disk's radial structure to the compact scenario.
Hence, by measuring the radial extent of the disk, we can comment on the formation scenarios of its central brown dwarf. We have also proposed to observe 12 brown dwarfs with protoplanetary disk in the Taurus star forming region through the Atacama Large Millimeter/sub-Millimeter Arrray (ALMA) cycle 2 observations.

CONTENTS

LIST OF FIGURES

LIST OF TABLES

ACRONYMS

SED Spectral Energy Distribution

SPH Smoothed Particle Hydrodynamics

IMF Initial Mass Function

CTTS classical T Tauri star

WTTS Weakly lined T Tauri star

ALMA Atacama Large Millimeter/sub-Millimeter Arrray

ALI Accelerated Lambda Iteration

MRI Magneto Rotational Instability

eVLA Extended Very Large Array

1 INTRODUCTION

1.1 HISTORY

1.1.1 *Nebular Hypothesis*

> Dieser Raum ist vollkommen leer, oder wenigstens so gut als leer; also muss er ehemals anders beschaffen und mit genugsam vermögender Materie erfüllt gewesen sein, die Bewegung auf alle darin befindliche Himmelskörper zu übertragen und sie mit der ihrigen, folglich alle unter einander einstimmig zu machen, und nachdem die Anziehung besagte Räume gereinigt und alle ausgebreitete Materie in besondere Klumpen versammlet: so müssen die Planeten nunmehr mit der einmal eingedrückten Bewegung ihre Umläufe in einem nicht widerstehenden Raume frei und unverändert fortsetzen.

Immanuel Kant in the 17^{th} century, mentions the above statement in his book "The Universal Natural History and the Theory of Heavens" (Kant, 1969). He argued that if planets in the solar system have coplanar orbits and most of them move in the same direction then there should have been an intermediate medium which should have regulated the motions of planets in the solar system. This theory is also known as the "Nebular Theory of planet formation".

Later, French Mathematician Pierre Simon Laplace used another version of the Nebular Hypothesis to account for the orbital motions of the planets and also their satellites in his book "The System of the World" (de Laplace, 1809). He argued that if the orbital motion of the satellite is same as the rotation of its host planet, they should have formed from the same rotating cloud. He assumes that the Sun should once have had a large atmosphere which extended beyond the solar system which then later collapsed to its present size.

Later in the 20^{th} century, systematic studies on planet formation were done based on Laplace's hypothesis. Ter Haar (1967) summarises various theories on the formation of Solar System.

1.2 BROWN DWARFS

Brown dwarfs are very low mass substellar objects whose masses are $<0.08M_\odot$. Their formation process is simmilar to that of low mass stars, but their final mass is too low to start hydrogen burning.

Brown dwarfs were first proposed by Kumar (1963) and Hayashi & Nakano (1963) through numerical models. They found out that pre-stellar cores below $0.08M_\odot$ ends up being completely convective. These objects also have non-relativistic degeneracy in their interiors. This degeneracy increases the efficiency of heat transport due to conduction which cools down the interiors to very low temperatures and thus preventing the object to begin nuclear fusion for its energy generation.

Kumar (1963) found out that the critical mass required for hydrogen burning also depends on the metallicity of the object. A population I object of metallicity of $Z = 0.03$, the critical mass is about $0.07M_\odot$ and for a population II object of metallicity of $Z = 0.01$ the critical mass is about $0.09M_\odot$.

The first brown dwarfs to be observed were Teide1, PP115 and Gliese 229B [Rebolo et al. (1995), Nakajima et al. (1995), Oppenheimer et al. (1995), Basri et al. (1996)]. Protoplanetary disks around young brown dwarfs were detected through excess in the H-K colors [Luhman (1999), Muench et al. (2001)]. However, brown dwarfs do not heat up the disks sufficiently at these bands to show a significant excess from the stellar SED (Luhman, 2012). Hence, with ground and space based telescopes at mid-infrared and at longer wavelengths like the Infrared Space Observatory(ISO), Herschel, Spitzer, etc. it is more easier to detect the excess above the photosphere SED (Harvey et al. (2012), Luhman et al. (2005), Apai et al. (2004)).

1.3 FORMATION OF BROWN DWARFS

The formation process of a brown dwarf is similar to that of any low mass stellar counterpart. There are several models proposed for the formation of very low mass stars and brown dwarfs.

1. Gravitational collapse and fragmentation of clouds into smaller fragments, the tidal shear and high velocities within the cloud stop accretion onto the low mass clumps ($\leqslant 0.08 M_{\odot}$) (Bonnell et al., 2008)
2. Due to dynamical interactions between the protostars within the core, smaller clumps get ejected from the cloud preventing further accretion (Reipurth & Clarke, 2001)
3. Photoionising radiation from a nearby OB star also halts accretion by removing the envelope and the disk of the low mass protostar (Whitworth & Zinnecker, 2004)
4. Gravitationally unstable massive disks around stars can produce low mass fragments in the disk forming low mass stars and brown dwarfs (Stamatellos & Whitworth, 2009)
5. Low mass clumps being produced in the cloud due to turbulent fragmentation of gas in the cloud (Padoan & Nordlund, 2002)

It is known that these models of brown dwarf formation are not mutually exclusive and can coexist. But from the perspective of the formation of protoplanetary disks around these stars, each model will result in different disk structures. Whitworth & Goodwin (2005) have reviewed the above processes in detail and we shall review them in the following subsections,

1.3.1 *Gravitational fragmentation*

At high gas densities in a collapsing molecular cloud, the jeans mass for collapse is sufficiently low to trigger formation of low mass stars and brown dwarfs.

$$M_{Jeans} = \frac{4\pi}{3}\rho R_{jeans}^{3} = \frac{\pi}{6}\frac{c_s^3}{G^{1/3}\rho^{1/2}} \tag{1}$$

High dense regions can also form by tubulence in the cloud. The turbulent fragmentation will be described in detail in sect.1.3.5. But gravity can be an efficient alternative to turbulence in forming high dense regions. Gravity has a better advantage over turbulence as it is intrinsically convergent and hence can compress gas into smaller volumes with larger densities. It is mostly found that low mass stars and brown dwarfs tend to form at the outskirts of stellar clusters. The gravitational potential of the cluster will shear the cloud and pull the gas from the collapsing fragments into the cluster potential. This increases the density locally and decreases the Jean's mass of that region and thereby forming more low mass stars and brown dwarfs.

1.3.2 *Ejection model*

When a low mass protostar encounters a multiple system of heavier stars/protostars, the dynamical interaction with the system will eject the low mass protostar and hence stop its accretion. Numerous SPH simulations show that ejection can occur in any scenario.

Fig.1 shows two different SPH simulations done by Bate et al. (2002) of brown dwarf formation. The ejected brown dwarfs are marked with triangles and squares. The top panels show formation of the brown dwarfs by disk fragmentation of a disk around a binary system. The lower panels show formation of the brown dwarfs in separate filaments, where they eventually fall into the central multistar system and then get ejected.

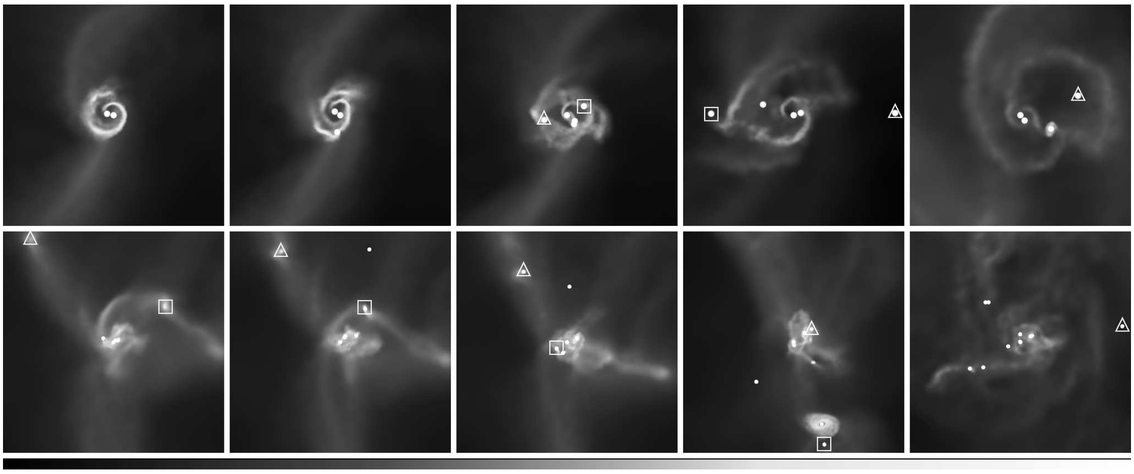

Figure 1: *SPH simulations of brown dwarf formation Bate et al. (2002).*

1.3.3 *Formation by photo-erosion*

This model put forth by Whitworth & Zinnecker (2004), explores another possibility of formation of rogue brown dwarfs and planetary mass objects. When a protostar collapses in the vicinity of an OB type star, the radiation from the OB star ionises the envelope of the protostar hence forming an ionisation front. This ionisation front erodes the material from the protostar's envelope, thus preventing it from further accreting mass to initiate hydrogen burning.

1.3.4 *Graviatational Instability*

Another possible scenario for the formation of low mass stars and brown dwarfs is the collapse of dense molecular clouds and massive circumstellar disk. For a circumstellar disk which has a large disk to stellar mass ratio, its gravity overcomes the thermal and centrifugal support and the cooling time of a fragment in the disk is lower than the orbital time so that the fragment can efficiently collapse. This makes the disk gravitationally unstable and thus forms smaller protostars which can end up as brown dwarfs or low mass stars. The top panel in Fig.1 shows the formation of two brown dwarfs through this process. Fig.2 shows the mass spectrum of an SPH simulation of a gravitationally unstable circumstellar disk by Stamatellos & Whitworth (2009), which illustrates that that this process can also make a significant number of low mass stars above the hydrogen burning limit.

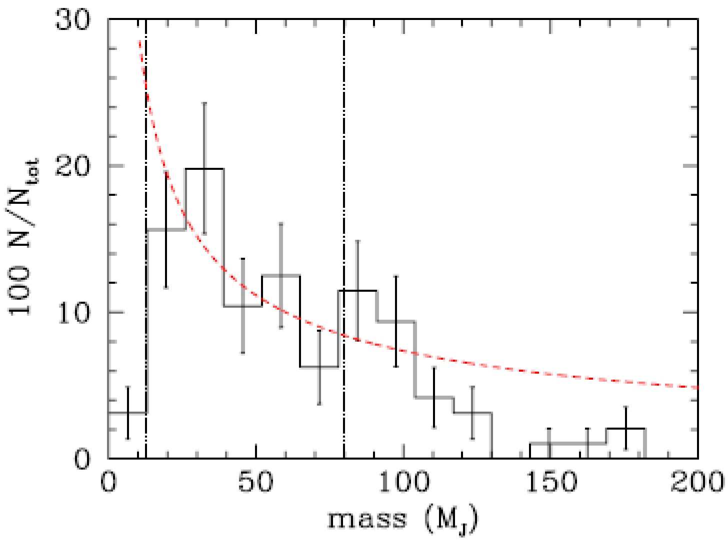

Figure 2: *Mass spectrum of objects produced by fragmentation of a 0.7* $M_\odot$ *disk around a 0.7* $M_\odot$ *star (Stamatellos & Whitworth, 2009). The vertical dotted lines show the deuterium burning limit (*$\approx 13 M_J$*) and the hydrogen burning limit (*$\approx 80 M_J$*). The red dashed curve shows the low mass IMF with* $\Delta N/\Delta M \propto M^{-0.6}$

1.3.5 *Turbulent fragmentation*

Another way to produce high dense regions in collapsing molecular clouds is by supersonic turbulence. Such supersonic turbulence fragments the cloud into dense sheets, filaments, cores and large low-density voids by highly radiative shocks.

Even though all these processes predict a different formation path for the low mass protostar. They can also coexist and a single protostar can be part of multiple scenarios during its formation. (Padoan & Nordlund, 2002)

1.3.6 *Impact on the structure of the protoplanetary disks*

Each formation process has its own consequence on the radial extent of the disk. If the star/-substellar object is ejected from the cloud due to dynamical interactions, the dynamical time scale will be smaller than the free fall time and hence the disk will be radially smaller than the disk around a low mass star/substellar object that is not ejected from the collapsing core. If the envelope is eroded by the ionising radiation from a nearby OB star, the low mass protostar can also lose its disk to the ionisation front. The radial extent of the protoplanetary disk can be physically estimated with molecular emission lines at sub-mm wavelengths and imaging the dust thermal emission in the far-IR to sub-mm wavelength range.

1.4 SPECTRAL ENERGY DISTRIBUTION (SED)

It is difficult to measure physical quantities of protoplanetary disks directly from observations and hence to classify them based on those quantities. Hence, as a first approach, it is better to classify protoplanetary disks based on their SED, which is a direct observable quantity.

The spectral energy distribution is the energy emitted by a source as a function of wavelength. Fig.3 illustrates on how various parts of the protoplanetary disk contributes to the SED.

The presence of a protoplanetary disk can be inferred from the excess in the infrared part of the SED. The slope of the SED between $2.2\mu m - 24\mu m$ (near- and mid-infrared regions)[1] can be used to classify the disks. The slope of the SED at these wavelengths is,

$$\alpha_{IR} = \frac{\Delta \log(\lambda F_\lambda)}{\Delta \log(\lambda)} = \frac{\Delta \log(\nu F_\nu)}{\Delta \log(\nu)} \quad (2)$$

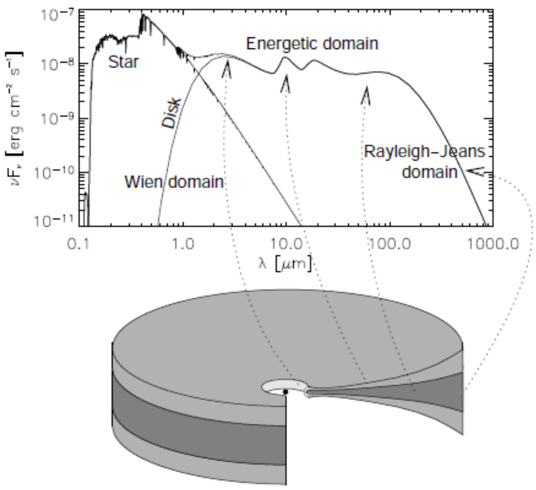

Figure 3: *Sources for various components of the SED from different parts of the protoplanetry disk. (Dullemond et al., 2007)*

1.4.1 *Classification of Protoplanetary disks*

Protoplanetary disks can be classified into four classes based on the value of α_{IR}. This way of classifying circumstellar disks by their IR slope was proposed by Lada & Wilking (1984). They classified them into three classes (I-II-III). As the sensitivities for the millimeter telescopes increased, Class 0 was introduced by Andre et al. (1993). Greene et al. (1994) subsequently introduced the "Flat Spectrum" class which is an intermediate between Class I and Class II objects.

- **Class 0**: These are protostars which have a collapsing envelope arround. The flux emitted is from the circumstellar material falls mostly in the far infrared part of the SED. They are undetectable at $\lambda < 20\mu m$.
- **Class I**: These are protostars which have a collapsing envelope and a forming disk around. Hence, the flux is significantly flat in the near and mid-IR part of the SED. Their α_{IR} is larger than 0.3.
- **Flat spectrum (FS)**: These objects are an intermediate between the class 0 and class I objects, where the IR slope is in the range $-0.3 < \alpha_{IR} < 0.3$. Their SED is flat throughout the entire infrared part.
- **Class II**: These are protostars which have an accreting disk around them. They show strong emission in Hα and in the UV, similar to a classical T Tauri star (CTTS). Their SED drops noticibly between near and mid IR with a slope in the range $-1.6 < \alpha_{IR} < -0.3$.
- **Class III**: These objects have more passive disks with very weak or no accretion simmilar to a Weakly lined T Tauri star (WTTS). Their IR flux originates only from the stellar photosphere and the value of α_{IR} is lesser than -1.6.

[1] near-infrared: $0.78\mu m - 5\mu m$
mid-infrared: $5\mu m - 25\mu m$

Class	SED slope	Mass distribution	Characteristics
0	-	$M_{envelope} > M_{star} > M_{disk}$	peak of SED falls in far-IR
I	$\alpha_{IR} > 0.3$	$M_{star} > M_{env} \approx M_{disk}$	flat SED at near and mid-IR
FS	$-0.3 < \alpha_{IR} < 0.3$	-	intermediate between class I and class II
II	$-1.6 < \alpha_{IR} < -0.3$	$M_{disk}/M_{star} \approx 1, M_{env} \approx 0$	Strongly accreting disk
III	$\alpha_{IR} < -1.6$	$M_{disk}/M_{star} < 1, M_{env} \approx 0$	Passive or weakly accreting disk

Table 1: *Classification of young stellar objects. (Williams & Cieza, 2011)*

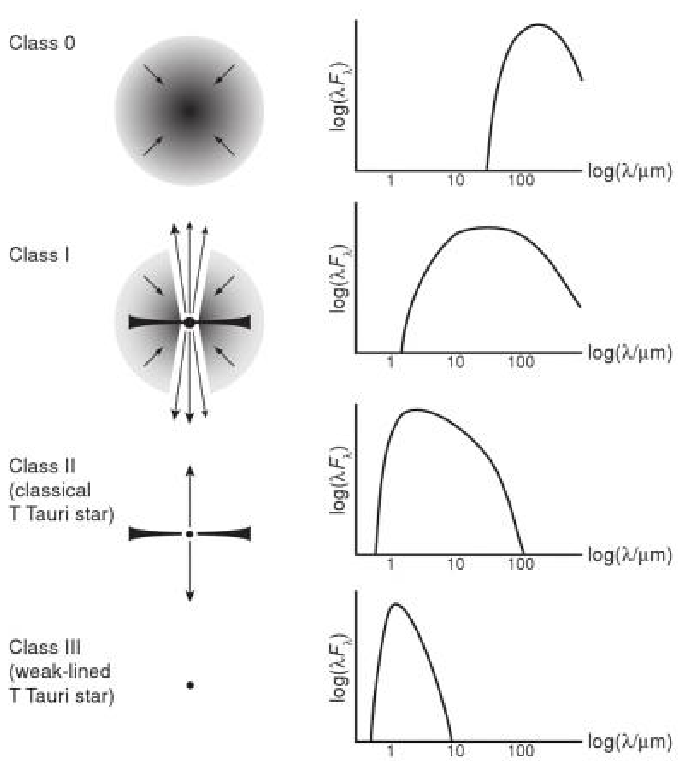

Figure 4: *Classification of young stellar objects based on their SED (Armitage, 2010)*

1.5 RADIATION THERMO-CHEMICAL MODELS

Protoplanetary Disk Model or ProDiMo is a detailed radiative transfer and thermo-chemical code, which uses global iterations to calculate the physical, chemical and thermal structure of a protoplanetary disk (Woitke et al., 2009). It includes 2D dust continuum radiative transfer, gas phase chemistry and photochemistry and solves the hydrostatic disk structure in axisymmetry. Fig.5 shows the iteration flow of ProDiMo.

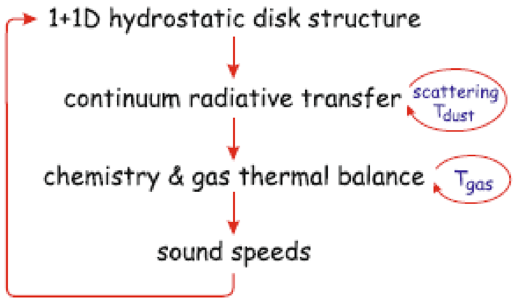

Figure 5: *Iteration flow followed in ProDiMo. The circular arrows indicate sub-iterations. (Woitke et al., 2009)*

1.5.1 *Hydrostatic Disk structure*

ProDiMo computes the hydrostatic disk structure in axial symmetry neglecting motions in the radial and vertical scale, i.e. $v_r = 0$ and $v_z = 0$. Hence, the equations of motion become,

$$\frac{v_\phi^2}{r} = \frac{1}{\rho}\frac{\partial p}{\partial r} + \frac{\partial \Phi}{\partial r} \tag{3}$$

$$0 = \frac{1}{\rho}\frac{\partial p}{\partial z} + \frac{\partial \Phi}{\partial z} \tag{4}$$

Where v_r, v_ϕ and v_z are the velocities in radial, azimuthal and vertical axes, P is the gas pressure and ρ is the mass density and Φ is the graviational potential of the central star.

Assuming that the radial pressure gradient is negligible compared to the centrifugal acceleration and gravity, the radial and vertical components of the equation and thus ProDiMo solves the hydrostatic equlibrium in 1+1D modelling.
Since the solutions for the radial components are circular kepplerian orbits, the radial distribution is determined by the angular momentum distribution. Hence, only vertical hydrostatic equilibrium has to be solved. The vertical structure is solved through an ordinary differential equation solver by substituting the density for the pressure through the isothermal sound speed (c_T). The isothermal sound speed is interpolated linearly between the grid points.

1.5.2 *Continuum radiative transfer*

ProDiMo solves for the local continuous radiation field J_ν and the dust temperatures T_D, which are essential for the chemistry and heating & cooling balance in the disk, through the radiative transfer equation,

$$\frac{dI_\nu}{d\tau_\nu} = S_\nu - I_\nu \tag{5}$$

where I_ν is the spectral instensity, S_ν is the source function and τ_ν is the optical depth.

The source function in LTE can be written as,

$$S_\nu = \frac{\kappa_\nu^{abs} B_\nu(T_D) + \kappa_\nu^{sca} J_\nu}{\kappa_\nu^{ext}} \tag{6}$$

Where κ_ν^{abs}, κ_ν^{sca} and κ_ν^{ext} are the absorbtion, scattering and extinction coefficients, B_ν is the planck function and J_ν is the mean intensity.

The external radiation field has two sources, the stellar and the interstellar irradiation. ProDiMo uses the PHOENIX models for stellar atmospheres to determine the stellar component. The UV fluxes can be deduced from observations or assuming a power law. This UV component is the cause for ionisation and dissociation of atoms and molecules in the disk. The interstellar radiation component is assumed to be isotropic and approximated by a highly diluted 20000K blackbody field and a 2.7K cosmic background black body. The UV field is computed by using the Draine radiation field given by Draine (1978) and Draine & Bertoldi (1996), setting the UV field strength $\chi = 1$ (Röllig et al., 2007).

The radiative transfer eq.5 can be solved at a particular point (r,z) in the disk by ray tracing and intergrating the eq.5 with the Λ iterations given by,

$$J_\nu = \Lambda_\nu[S_\nu] \tag{7}$$

where Λ is a matrix operator acting on the source function to result in the mean intensity J_ν.

solving the continuum radiative transfer by the simple Λ iteration can take too much time to converge. Hence, ProDiMo uses the Accelerated Lambda Iteration (ALI) (Auer, 1984), where the Λ operator can be written as,

$$\Lambda = \Lambda^* + (\Lambda - \Lambda^*) \tag{8}$$

where Λ^* is a chosen approximate Λ operator and hence equation 7 becomes,

$$S_\nu^{(n+1)} = \Lambda^* S_\nu^{(n+1)} + (\Lambda - \Lambda^*) S_\nu^n \tag{9}$$

Thus the initial simple Λ operator splits into two components, the chosen approximate Λ^* operator on the new iterated value for S_ν and the difference between the initial value for Λ and Λ^* acting on the current value of S_ν.

With the right choice for the Λ^* operator, the solution for eq.5 will converge faster.

1.5.3 *Chemistry*

The chemistry in ProDiMo involves 9 elements (H, He, C, N, O, Mg, Si, S, Fe) and 71 atomic, ionic, molecular and ice species. The reaction rates for 911 chemical reactions are taken from the UMIST 2006 database (Woodall et al., 2007). Out of the total 950 reactions, there are 74 photo-reactions, 177 neutral-neutral rections, 299 ion-neutral reactions, 209 charge-exchange reactions, 46 cosmic ray induced photoreactions and 26 three body reactions. The other 39 reactions include UV-photoionisation, H_2 formation on grains, excited H_2 chemistry and formation and evaporation of ice. The rates for these reactions are derived exclusively from other literature.

The net formation rate of a chemical species i is,

$$\begin{aligned}\frac{dn_i}{dt} = &\sum_{jkl} R_{jk\to il}(T_g) n_j n_k + \sum_{jl} (R^{ph}_{j\to il} + R^{cr}_{j\to il}) n_j \\ &- n_i \left(\sum_{jkl} R_{il\to jk} n_l + \sum_{jk} (R^{ph}_{i\to jk} + R^{cr}_{i\to jk}) \right)\end{aligned} \tag{10}$$

Where $R_{jk\to il}$ is the rate for two body gas phase reactions, $R^{ph}_{j\to il}$ indicates a photo-chemical reaction rate and $R^{cr}_{j\to il}$ indicates a rate of a cosmic-ray induced reaction.

1.5.3.1 *Photo-chemistry*

A detailed computation of photo-chemistry involves detailed radiative transfer and molecular opacities for self-sheilding. ProDiMo computes the rates for photochemistry by using the spectral energy density from the 2D continuum radiative transfer and the reaction cross-sections from the Leiden database (van Dishoeck et al., 2008).

1.5.4 *Gas thermal balance*

The gain in thermal kinetic energy due to various heating and cooling processes is given by,

$$\frac{de}{dt} = \sum_k \Gamma_k(T_g, n_{sp}) - \sum_k \Lambda_k(T_g, n_{sp}) \tag{11}$$

Where Γ_k and Λ_k are the heating and cooling rates. In order to have a thermal balance we have to set de / dt = 0, thus eq.11 gives an inplicit relation for T_g. But heating and cooling rates also depend on the particle densities n_{sp}, which in turn depend on the gas temperature T_g. Hence, the heating and cooling rates are iterated and the chemistry is solved again until T_g satisfies the thermal balance.

1.5.5 *Sound speeds*

After computing the gas temperatures (T_g) and particle densities n_i, ProDiMo updates the isothermal sound speeds required for the next iteration of the hydrostatic disk structure using,

$$\rho = n_e m_e + \sum_i n_i m_i \tag{12}$$

$$p = \left(n_e + \sum_i n_i \right) kT_g \tag{13}$$

$$c_T^2 = P/\rho \tag{14}$$

The isothermal sound speed derived in eq.14 is used to iterate on the hydrostatic disk structure and thus repeating the global iterations of ProDiMo until the vertical structure of the disk is converged.

1.6 GOAL OF THIS THESIS

Brown dwarfs have a formation process that is similar to that of the low mass stellar counterparts. However during their formation, they are affected by numerous other physical processes such as gravitational instability, ejection from the star forming region, photo-erosion due to a nearby O type star, etc. These processes also affect the structure and chemistry of the circumstellar material around the brown dwarfs. In this thesis, I want to investigate the physical structure and chemistry of a protoplanetary disk around a typical brown dwarf and compare them to protoplanetary disks around standard T Tauri and Herbig stars with analytical and numerical models. Based on my first results, I proposed to observe 12 brown dwarfs with protoplanetary disk in the Taurus star forming region with the Atacama Large Millimeter/Sub-Millimeter array (ALMA), Chile. The observations would be used to constrain the analytical and numerical models by measuring for the first time the radial extent of a meaningful sample of disks, and thus provide new insights into their formation paths.

2 ANALYTIC MODELS

2.1 NEED FOR ANALYTIC MODELS

Protoplanetary disk structure to the first order could follow a regular trend in its evolution with stellar mass. These trends can be deduced from analytic models constrained by simple assumptions. These models can also provide an initial understanding on the structure of protoplanetary disks around different stars. They can also reduce the degeneracies in Spectral Energy Distribution fitting by constraining the parameter space for the fit.

The output of these analytic models are mostly driven by the properties of the central star like stellar radiation, stellar mass, etc. These parameters are the major driving forces for the heating and cooling of dust and gas in the disks and the vertical scale height due to gravity. Hence, they also affect the hydrostatic equilibrium of the disk. Thus, an analytic model which calculates the overall struture of the disk with respect to the properties of the central star will directly show us how the strucutre changes for different types of central stars. Hence, to compare the structure of a brown dwarf protoplanetary disk with that of a T-Tauri and a Herbig star, these analytic models will be a good tool to analyze the global differences in their structure.

2.2 ASSUMPTIONS

To reduce the complexity in the analytic equations and to reduce the number of free parameters to mostly that of the central star, we make the following assumptions in our models. In our analytic models we neglect all dynamic effects like mass accretion, viscosity, turbulence, etc. and assume that all our disks are passive.

2.2.1 *Temperature and Surface density*

The temperature is measured around the midplane of the disk. Also, they follow a power law distribution radially in the disk. The disks are assumed to be isothermal on the vertical scale. The radial distribution of temperature and surface density in the disk is given by,

$$T = T_0 \left(\frac{R}{R_{in}} \right)^{-0.25} \tag{15}$$

$$\Sigma = \Sigma_0 \left(\frac{R}{R_{in}} \right)^{-\epsilon} \tag{16}$$

The exponent of temperature power law is found through detailed 2 dimensional radiavtive transfer disk model by using the DENT grid as 0.25. (Kamp et al. (2011), Woitke et al. (2010)

2.2.2 *Inner radius*

We assume that the inner radius of the protoplanetary disk is where the dust grains start to condensate. This happens at a temperature of 1500K. Hence assuming,

$$R_* T_*^2 = R_{in} T_{cond}^2 \tag{17}$$

$$R_{in} = \sqrt{\frac{L_*}{4\pi\sigma_{SB}T_{cond}^4}} \tag{18}$$

We can deduce the inner radius by setting the temperature at that point to the dust condensation temperature.

2.2.3 *Gravitational Stability*

To model the surface density using the assumption given by eq.16, we have to estimate the surface density at the inner radius (Σ_0). One of the ways of computing the surface density at the inner radius is by finding the critical surface density where the disk becomes just gravitationally stable against the gravity of the central star. This is given by the Toomre's criterion,

$$Q = \frac{\kappa(r)c_s(r)}{\pi G\Sigma(r)} \tag{19}$$

Where c_s is the sound speed, G is the graviational constant, Σ is the surface density and κ is the epicyclic frequency and is given by,(reference needed)

$$\kappa(r) = \frac{1}{r^3}\frac{d(r^4\Omega(r)^2)}{dr} \tag{20}$$

Where Ω is the orbital frequency and assuming that the disks orbit in keplerian rotation,

$$\Omega_{kep} = \sqrt{GM_*/r^3} \tag{21}$$

Using assumptions given in eq.15 and eq.16 the surface density as a function of disk mass, inner and outer radii becomes,

$$\Sigma_0 = \frac{M_{disk}(2-\epsilon)}{4\pi R_{in}^2}\left(\left(\frac{R_{out}}{R_{in}}\right)^{(2-\epsilon)} - 1\right)^{-1} \tag{22}$$

Where, M_{disk} is the disk mass, ϵ is the surface density exponent given in eq.16 and R_{out} is the outer radius of the disk. By setting r in eq.19 to R_{out} and Q = 1 for the solution to be just gravitationally stable, we can estimate the outer radius of the disk as,

$$R_{out} = R_{in}\left(\frac{M_{disk}(2-\epsilon)}{4\pi}\sqrt{\frac{A}{T_0 M_* R_{in}}}\right)^{8/3} \tag{23}$$

Where,

$$A = \frac{\mu m_H G\pi^2}{k} \tag{24}$$

and μ is the mean molecular weight and for a typical solar abundance the value of $\mu \approx 2.4$ (Stahler & Palla, 2008), m_H is the mass of hydrogen and k is the Boltzman's constant. Andrews & Williams (2007) found from a sample of T Tauri disks in Taurus-Auriga and Ophiuchus-Scorpious regions that the outer radius is $\approx$ 200AU for these objects. Also, Ricci et al. (2012) found from ALMA observations of ρ-Oph 102 brown dwarf that the disk is about 40 AU in sub-mm continuum. We can assume these as the standard values for the outer radii expected from the analytic models.

In eq.23, the disk is set to be just gravitationally stable which means the surface density is at the highest possible value and hence the disk gets smaller than what is expected for any standard value of ϵ. Hence, to get reasonable value for the outer radius and surface density at inner radius, we have to scale down the surface density at inner radius to a value that is β times the critical value (β«1) and thus eq.23 becomes,

$$R_{out} = R_{in} \left(\frac{1}{\beta} \frac{M_{disk}(2-\epsilon)}{4\pi} \sqrt{\frac{A}{T_0 M_* R_{in}}} \right)^{8/3} \tag{25}$$

The value of β can be set by calibrating the outer radius with that of the observed outer radii mentioned above.

2.2.4 *Disk Mass*

Mohanty et al. 2013 found from bayesian analysis of SCUBA-2 observations of low-mass stars and brown dwarfs that the disk to stellar mass ratio follows the relation,

$$M_{disk} = (3.98 \times 10^{-3}) \times M_* \tag{26}$$

2.2.5 *Scale Height*

The scale height at any radial point r for a stationary accretion disk is given by, (Pringle 1981)

$$H(r) = \sqrt{\frac{kT(r)r^3}{\mu m_p G M_*}} \tag{27}$$

Where T(r) is the dust temperature at the radial distance r from the star and m_p is the mass of a proton.

2.3 MASS TO LIGHT RATIO

To build analytic models from the above mentioned assumptions, we need to define a set of input stellar parameters namely mass and luminosity. Hence, to begin with we can assume a simple mass to light ratio for a sample of stars given by,

$$\frac{L_*}{L_\odot} = \left(\frac{M_*}{M_\odot} \right)^{\alpha} \tag{28}$$

Where,

$$\alpha = 1.8, \quad M_* < 0.3 M_\odot$$
$$\alpha = 4.0, \quad 0.3 M_\odot < M_* < 3.0 M_\odot$$
$$\alpha = 2.8, \quad M_* > 3.0 M_\odot$$

With the above mass to light ratio, we can derive the analytic models from the given assumptions. For example, using the assumption in eq.18 and replacing the stellar luminosity with the stellar mass from eq.28,

$$R_{in} = \sqrt{\left(\frac{M_*}{M_\odot}\right)^{\alpha} \frac{L_\odot}{4\pi\sigma_{SB}}} \tag{29}$$

$$R_{in} = 0.069 \left(\frac{M_*}{M_\odot}\right)^{\alpha/2} \text{ in AU} \tag{30}$$

Fig.6 shows the results of the power law models on the evolution of various disk structure parameters with its stellar mass.

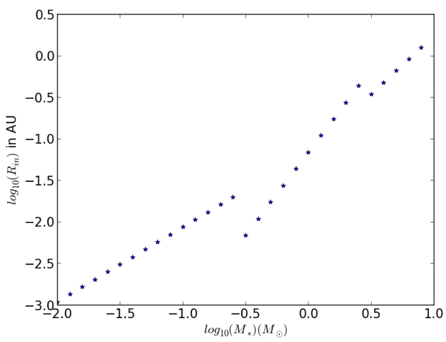

(a) *Inner radius*

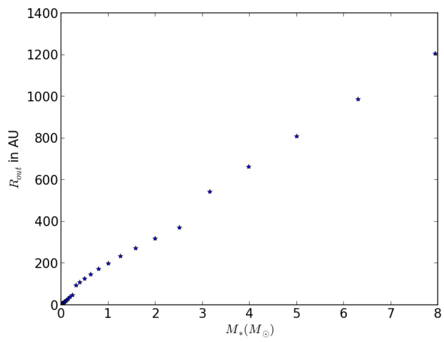

(b) *Outer radius*

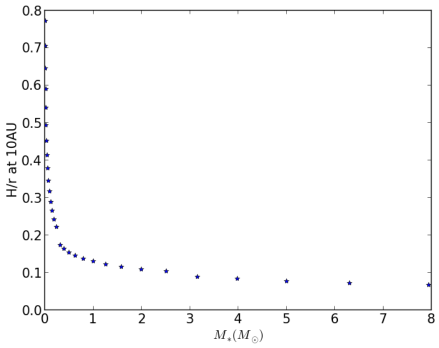

(c) *Scale height at 10AU*

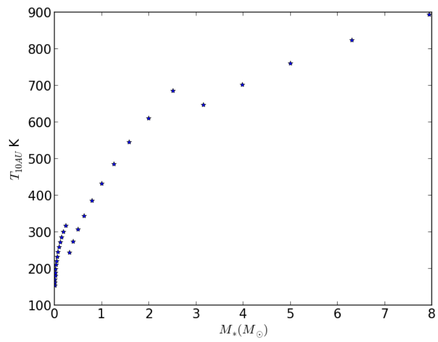

(d) *Temperature at 10AU*

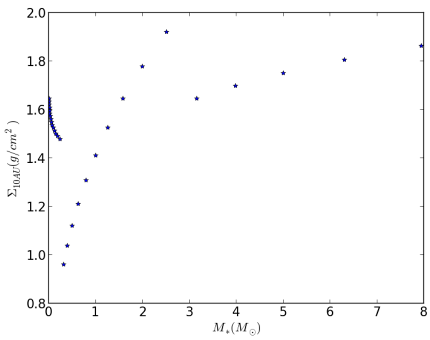

(e) *Surface density at 10AU*

Figure 6: *Analytic models for different quantities as a function of stellar mass using simple power law mass-to-light ratios*

2.3.1 *Problems*

Since the mass to light ratio is in three stellar mass regimes, we can see in fig.6 that the distribution has points of discontinuity and in some plots this discontinuity is pronounced (see for example fig.6e). Also the mass-to-light relation is for main-sequence stars, hence while the protoplanetary disks are found around pre-main sequence stars, hence we have to account for the stellar age in the mass-to-light ratio.

2.4 STELLAR EVOLUTION MODELS

The discontinuity in the models can be solved by using the pre-main sequence isochrones from the Pisa stellar evolution code (Tognelli et al., 2011) or stellar evolution models of Siess et al. (2000). The isochrones are in the age of 1Myr.

The Siess et al. (2000) model is an update to the Grenoble stellar evolution code, where they have changed the equation of state (EOS) to incorporate electron degeneracy in the models. Their models are in the mass range of $0.1M_\odot$ to $7.0M_\odot$ with 4 different metallicites (Z = 0.01, 0.02, 0.03, 0.04) and solar composition. The Pisa pre-main sequence models are an update to all the ealier pre-main sequence isochrones with wide range in metallicities (Z=0.0002-0.03) and masses from $0.2M_\odot$ to $7.0M_\odot$.

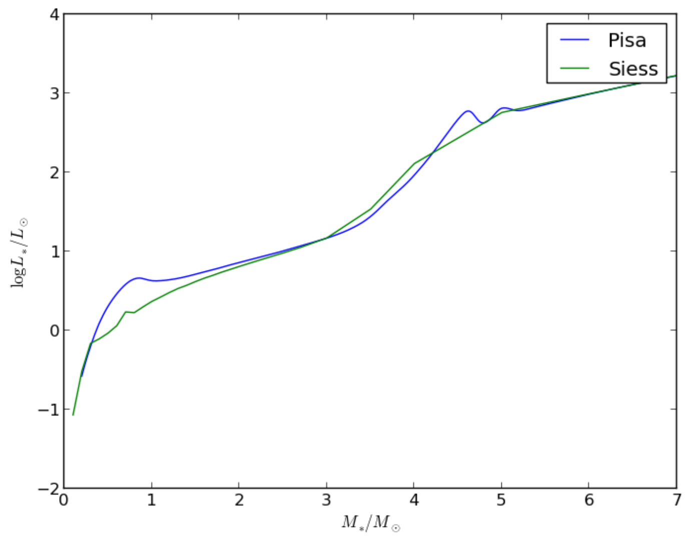

Figure 7: *Mass to Luminosity relation from Pisa (Tognelli et al., 2011) and Siess et al. (2000) models for 1Myr*

Fig.7 plots stellar luminosity against the stellar mass for an stellar evolution isochrone of age 1Myr from both Pisa and Siess et al. (2000) stellar evolution code.

2.5 RESULTS

By changing the input parameters from the discrete power law mass-to-light relation to the continuous pre-main sequence isochrones, the discontinuity in the models disappeared. For a surface density distribution of $\epsilon = 1.0$, the resulting analytic models are shown in fig.8. In fig.8, we see that both isochrones result in very similar quantities as a function of stellar mass. The next step is to compare the results from these analytic models to that of a detailed radiative transfer and thermo-chemical model (ProDiMo) which is described in chapter 3.

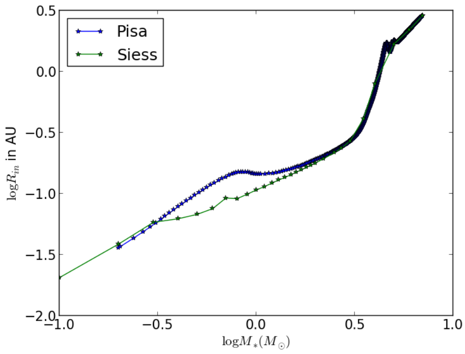

(a) *Inner radius*

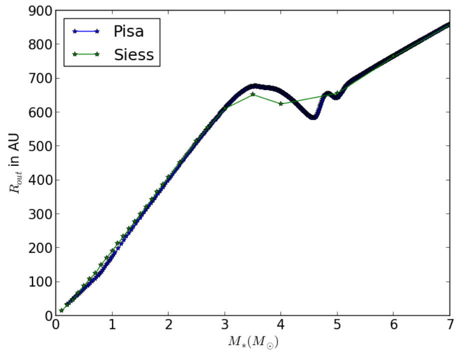

(b) *Outer radius*

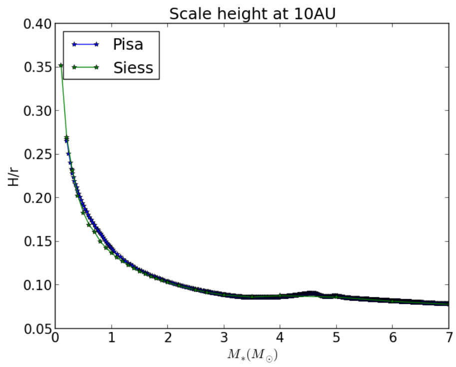

(c) *Scale height at 10AU*

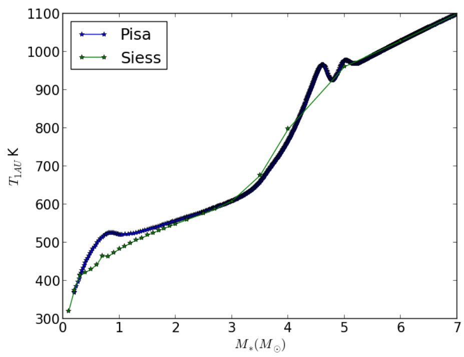

(d) *Temperature at 10AU*

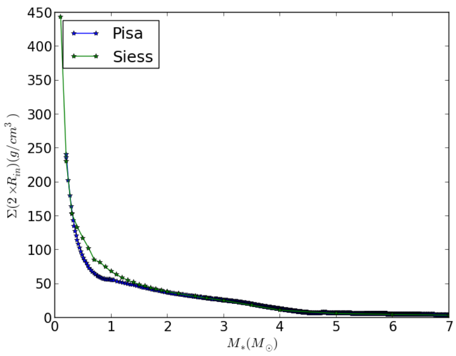

(e) *Surface density at 10AU*

Figure 8: *Analytic models of different quantities as a function of stellar mass using pre-main sequence isochrones of 1Myr*

Fig.8 shows us that the protoplanetary disk structure to the first order does depend mostly on the luminosity and the mass of its central star.

In fig.8d, we see that the temperature at any point in the disk (10AU in this case), increases with the central stellar mass and thus its luminosity. This effect is also evident in fig.8a for the inner radius of the disks. The region of the disk where the temperature is the dust condensation/sublimation temperature moves further outwards for heavier and brighter central stars. Thus the inner radius of the disk also moves out for a heavier/brighter central object.

As the central stellar mass increases, the disk mass also increases proportionally. Hence, to have a gravitationally stable disk, the radial size of the disk (R_{out} for example) should increase for heavier stars. This is seen in fig.8b. As the disk gets more radially extended the dust also spreads through out the disk and thus the surface density at any given point in the protoplanetary disk is lower for heavier stars as seen in fig.8e.

Finally, fig.8c shows us that as the central star gets heavier, the dust can efficiently settle down in the midplane due to the gravitational force. Hence, the scale height at any point in the disk is lower for disks around heavier stars.

However, to test the accuracy of the analytic results described above, we have to compare them with more detailed models and observations. In the upcoming sections, I shall discuss the results of radiative transfer and thermo-chemical models of protoplanetary disks (ProDiMo) to test the results of the analytic models described above with detailed 2D continuum radiative transfer and gas heating/cooling balance through ProDiMo models.

3 DETAILED NUMERICAL MODELS

The relations derived from the analytic models are continuous with stellar mass. However, the assumptions made in those models are quite simple, i. e.a power law distribution over the radial direction for Temperature and Surface density. Hence, in this chapter we will verify the results of the analytic models derived in chapter 2 with numerical models by solving detailed 2D continuum radiative transfer and the chemical heating/cooling balance in ProDiMo.

We ran five models using ProDiMo (Woitke et al., 2009) for protoplanetary disks around stars of central mass of $0.1M_{\odot}$, $0.7M_{\odot}$, $3.0M_{\odot}$, $5.0M_{\odot}$ and $7.0M_{\odot}$. The input parameters for the ProDiMo models i. e., stellar mass, luminosity, disk mass (M_{disk}), inner radius (R_{in}) and outer radius (R_{out}) are extracted from the analytic models. ProDiMo then solves for the temperature at each point in the disk through 2D continuum radiative transfer (T_{dust}). It also computes the scale height by solving for the vertical hydrostatic structure and the chemical heating/cooling balance (to solve for T_{gas} and thus the isothermal sound speeds) iteratively as described in sect.1.5.

The reults from ProDiMo was then compared with the result of the analytic models.

3.1 SCALED COORDINATE SYSTEM

A particular physical distance can point to different regions for disks around different stars. For example, 10AU in a T-Tauri disk, will be mostly the inner disk possibly within a shadow region of a puffed up inner rim, whereas for a brown dwarf or low mass star, 10AU can fall into the outer disk (fig.9a).

Hence, to compare the disk structure at a particular point in the disk for different types of central stars, it is better to scale all the models radially such that any point in this new scaled coordinate system will point to the same region in the disk. This will make the comparison easier across stellar types. For our new scaled coordinate system, we choose the inner radius as a reference point to scale the radial coordinates in the disk. Hence, a point which is two times as far as the inner radius in a brown dwarf disk will point at similar region around a T-Tauri or a Herbig disk (fig.9b).

This choice of coordinate system applies only to a selected few quantities. For example, the dust temperature in the midplane of a disk as shown in eq.15 is constant at any point scaled with the inner radius around any central star, assuming that the inner radius is at the dust condensation temperature. Hence, for a comparison of dust temperature in disks around stars with different stellar masses. We used the regular coordinate system of distance in astronomical units.

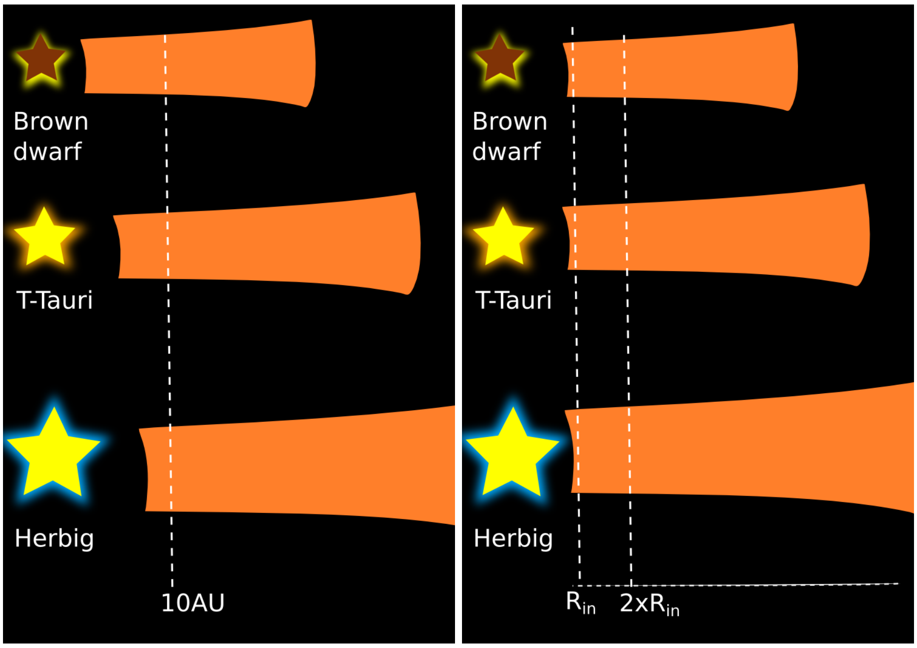

Figure 9: *sample location in a scaled(right) and unscaled(left) coordinate system.*

3.2 SCALE HEIGHT

By following the two layer model of Chiang & Goldreich (1997), i. e.a cold and dense midplane and a warm and optically thin upper surface, we can define two different scale heights for the protoplanetary disks.
The surface scale height (H_{surf}) is measured in the region where the disk gets optically thin to radiation. Hence, the surface scale height can be computed in the region $max(A_V)$ to $min(A_V) \approx 0.001$.The scale height in the midplane can be computed in the region where the density(n_H) goes from maximum to a density of $max(n_H)/e$. It can also be computed from the isothermal sound speeds in the midplane by,

$$H(r) = \sqrt{\frac{r^3 c_T^2}{GM_*}} \tag{31}$$

These two scaleheights are related by a ratio χ, given by

$$H_{surf}(r) = \chi H(r) \tag{32}$$

Typical values for χ are between 2 and 6. χ depends on the surface density (Σ) and the Planck mean opacity (κ_p).

As the temperatures used to compute the scale height in the analytic model are the midplane dust temperatures, we chose to compare them with the midplane scale height from the ProDiMo models. Also, as the scale height in the analytic models assume a hydrostatic equilibrium condition, we choose the pressure scale height computed from the isothermal sound speeds in the midplane from ProDiMo. The scale heights for $0.1 M_\odot$, $0.7 M_\odot$ and $3.0 M_\odot$ models mentioned above are shown in fig.10.

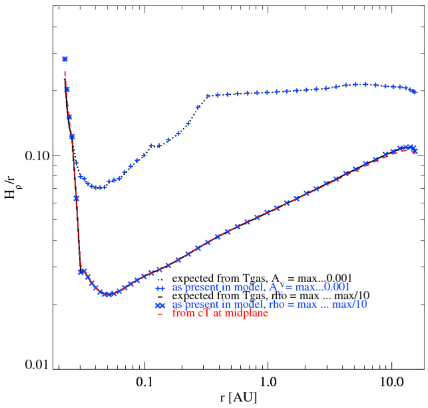

(a) $0.1 M_\odot$

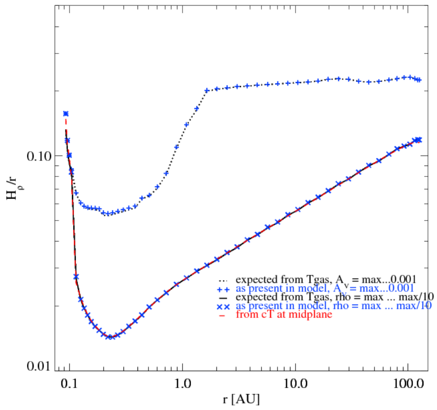

(b) $0.7 M_\odot$

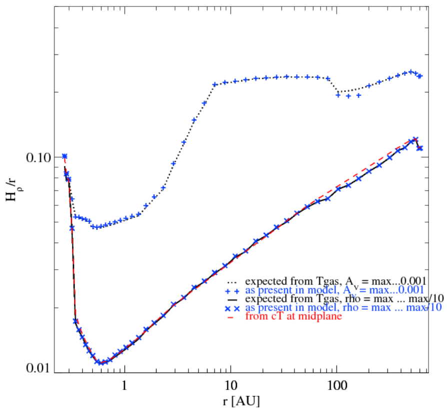

(c) $3.0 M_\odot$

Figure 10: *Scale heights measured from different ProDiMo models*

3.3 RESULTS

The temperatures were extracted at a distance of 10AU in the midplane from the five ProDiMo models. They match the same trend with stellar mass as that in the analytic models for the same distance of 10AU. The midplane scale heights in the ProDiMo models at a distance of $2 \times R_{in}$ also follow the same trend as that computed from the analytic models. These are shown in fig.11 & fig.12. An offset of a factor of 2-10 in temperature is found between the analytic and ProDiMo models, which is described in sect.3.3.1.

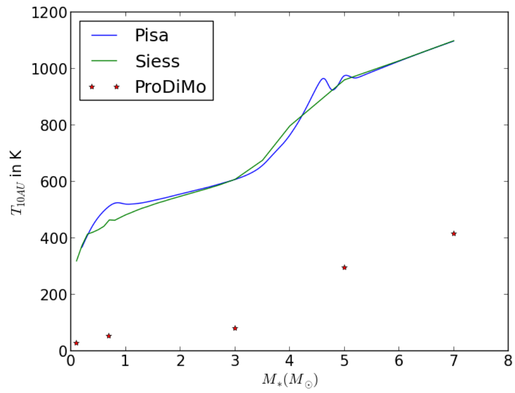

Figure 11: *Dust temperature at 10AU from both the analytic models and from ProDiMo*

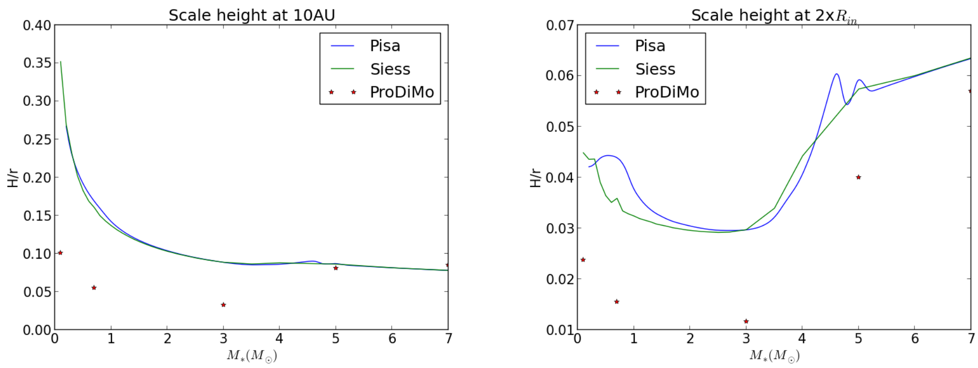

(a) *10AU* (b) $2 \times R_{in}$

Figure 12: *Scale height of the analytic models compared to that from ProDiMo*

3.3.1 *Offsets between the ProDiMo and analytic m*

As seen in fig.11 & fig.12, even though the trends match exactly, there seems to be an offset in the values by a factor of 2-10 in temperature. This is because of the highly optically thick inner region. This inner region which is the inner puffed up ring and its shadow are completely optically thick in the midplane. This leads to a steep dust temperature gradient in the midplane in this region which cannot be captured by a simple radial power law. The disk then follows further out a radial power law decrease in the midplane dust temperature. This region is shaded blue in fig.13.

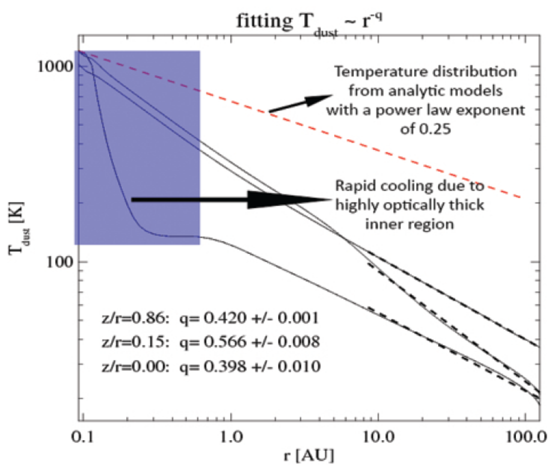

Figure 13: *Radial dust temperature profile at different scale heights of the* $0.7M_\odot$ *ProDiMo model. The red dashed line shows the power law trend from the analytic models. The shaded blue region marks the highly optically thick inner region*

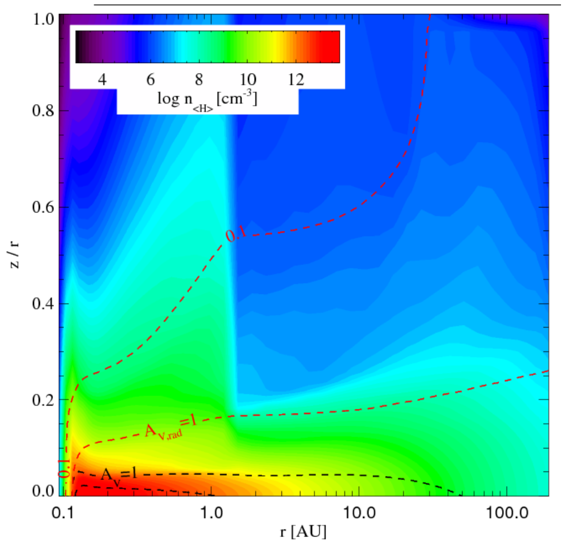

Figure 14: *Volume density distribution in a* $0.7M_{\odot}$ *disk with Thermo-Chemical bistability at* $\sim 1.5AU$ *overplotted with the visual extinction contours*

This steep decrease in the dust temperatures can also be affected due to various other processes in the inner disk, such as accretion, thero-chemical bistability, etc. These processes are still highly debatable. Accretion can heat and physically extend the inner bump thus raising the gas temperatures in this region. Thermo-chemical bistability is a phenomenon where the disk goes from being purely atomic to molecular. At a certain temperature/distance from the inner radius the atoms in the inner disk start to react with each other and form molecules. These molecules are more efficient in cooling the gas in the disk, thus a more efficient cooling can occur when the disk undergoes this transition. fig.14 shows this effect on the T Tauri model. After the inner bump the disk is still being heated at higher scale heights and the material is thus more vertically extended and after a distance of $\approx 1.5AU$ the molecules start to form and cool down the disk more rapidly this leads to lower gas scale heights. This effect of chemical heating has not yet been observed in any protoplanetary disk. However, it shows a significant effect on the vertical structure in our models.
The power law decrease of the dust temperature in the outer region of the disk can also vary due to other factors that affect the outer disk's temperature. For example, viscous force between the material in the midplane that tend to move inwards in the disk and the outflowing material higher up in the disk causes heating in the inner parts of the disk and thus increasing the slope of the temperature profile.

3.3.2 *Corrections for the observed offsets*

Correcting for the offsets by including the processes mentioned above in sect.3.3.1, will add more complexity to the analytic models and also additional dependencies on the disk structure. Since, the main goal is to model the scaling of disk structure only with the stellar mass and luminosity, we adpoted an empirical fudge factor in our ProDiMo models to account for the offsets in both temperature and scale heights. This fudge factor can be computed as the ratio of the dust temperatures from the analytic values to that from ProDiMo. As the scale height depend on the square root of the temperature, from eq.27, the correction for scale heights will be square root of the temperature correction factor. By adopting the fudge factor into the analytic models over dust temperature, the scale heights also seem to converge for the analytic and ProDiMo values.

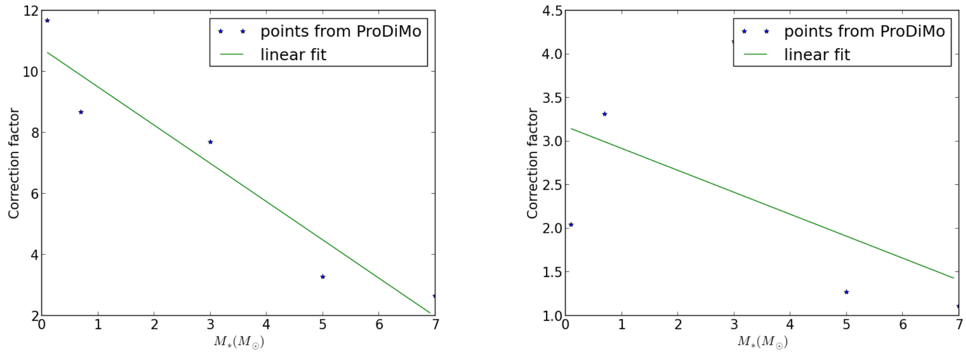

(a) *10AU* (b) $2 \times R_{in}$

Figure 15: *Temperature correction factor at the given distance as a function of stellar mass*

The offsets in fig.15 show a linear trend and thus can be fitted by a first order polynomial. The offsets are then applied to the scale heights with their square roots. The trends with the parameters corrected for the offsets are shown in fig.16 & fig.17.

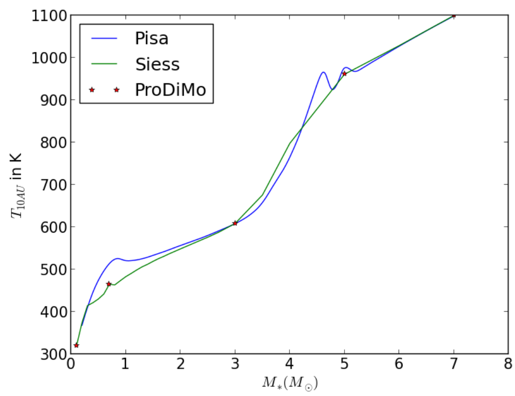

Figure 16: *Temperature corrected with the offsets*

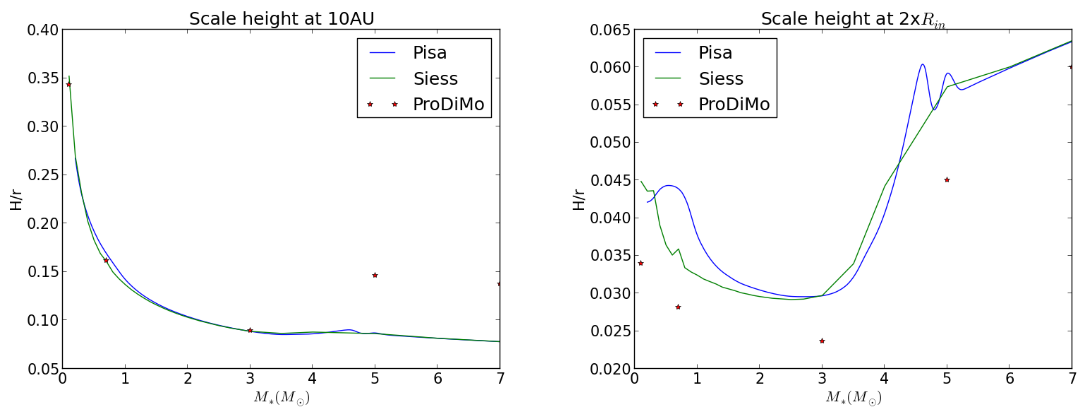

(a) *10AU* (b) $2 \times R_{in}$

Figure 17: *Scale heights corrected with the offsets*

3.4 DISCUSSION

In fig.16 and fig.17 it is evident that even though there are other physical processes like chemical heating and cooling, accretion, viscosity, etc. on smaller scales, the disk's radial and vertical structure depends mainly on stellar mass and luminosity.

Comparing the brown dwarf disk model of ProDiMo to that of a T-Tauri and a Herbig disk, we can infer that to the first order the brown dwarf disk is similar to a scaled down version of a T-Tauri or a Herbig disk. This is clearly visible in the volume density distribution of gas in these disks as shown in fig.18.

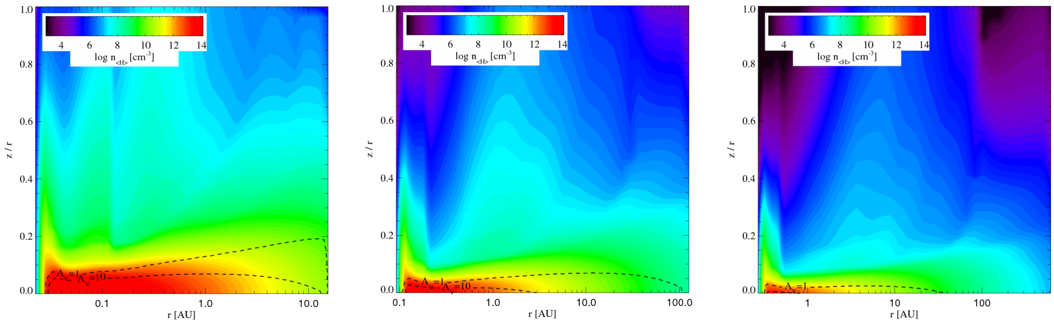

(a) *Brown dwarf* (b) *T Tauri* (c) *Herbig star*

Figure 18: *Volume density distribution as a function radius and scale height overplotted with visual extinction contours (Black dashed lines)*

The vertical strcutre of a protoplanetary disk is set by the vertical component of the stellar gravity, which depends on the stellar mass and the temperature in the disk. The latter depends on the stellar radiation. The high density region ($> 10^{12}\text{cm}^{-3}$) in the brown dwarf disk is more vertically extended than in T-Tauri and Herbig disks. This is because the verticlal component of the stellar gravity is significantly lower in brown dwarf disks than in T-Tauri and Herbig disks. The temperature of the disk, i.e.heating due to the stellar radiation, tends to extend the disk vertically. As the stellar mass increases the vertical component of gravity take over and pulls back the material to the midplane of the disk. Thus the scale height at any reference point in the scaled coordinate system decreases with stellar mass till $\sim 3.0M_\odot$. In the high mass regime the stellar radiation starts to dominate again in vertical disk structure. Hence, the trend in the scale height starts to rise again. This is more clearly visible in fig.12b in both the analytic trend and the trend from ProDiMo.

The effect of stellar mass on the inner regions of the disk can also be seen in fig.19. As CO is one of the most abundant molecular gas in the disk they are excellent tracers for gas through out the disk. The shadow due to the inner puffed up rim gets more extended as the stellar mass increases. As the heavier stars tends to heat up the inner regions more efficiently thus puffing up the inner rim and thus increasing its shadow on the disk.

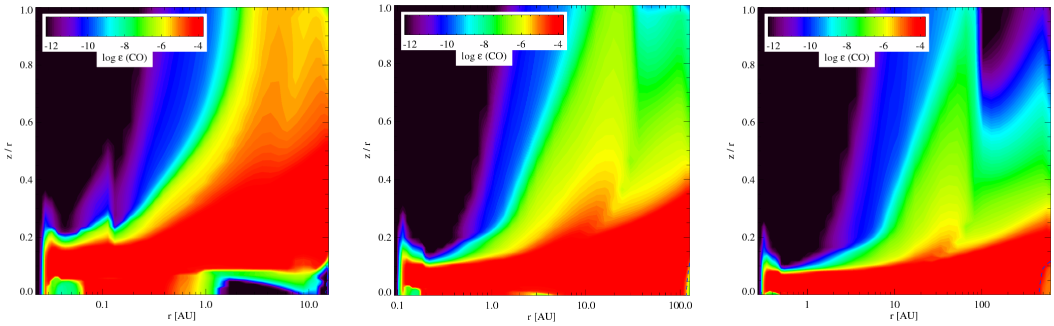

(a) *Brown dwarf* (b) *T Tauri* (c) *Herbig star*

Figure 19: *Distribution of equilibrium abundance of Carbon Monoxide (CO) over radius and scale height*

4 SED ANALYSIS

4.1 MEAN BROWN DWARF SED

To have a detailed comparison on the structure and chemistry of a protoplanetary disk around a brown dwarf with that of a T Tauri and Herbig star, we need a good representative model of a typical brown dwarf protoplanetary disk. Since the first detection of brown dwarfs in 1995 (Rebolo et al. (1995), Nakajima et al. (1995)), there has been a significant number of brown dwarfs with protoplanetary disks have been observed. Since the SED is the first tool to determine the physical properties of protoplanetary disks, an SED constructed by taking a mean of the photometric points for a sample set of brown dwarfs with proroplanetary disk is a good representative for the SED of a typical brown dwarf with protoplanetary disk.

In my study, I chose a sample of 14 brown dwarfs with protoplanetary disks in the Taurus star forming region. The photometric points were retrieved from Guieu et al. (2007) and Harvey et al. (2012). The photometric points from the above mentioned sources are tabulated in table 2. The mean of all the 14 sources with their induvidual photometric points is shown in fig.20.

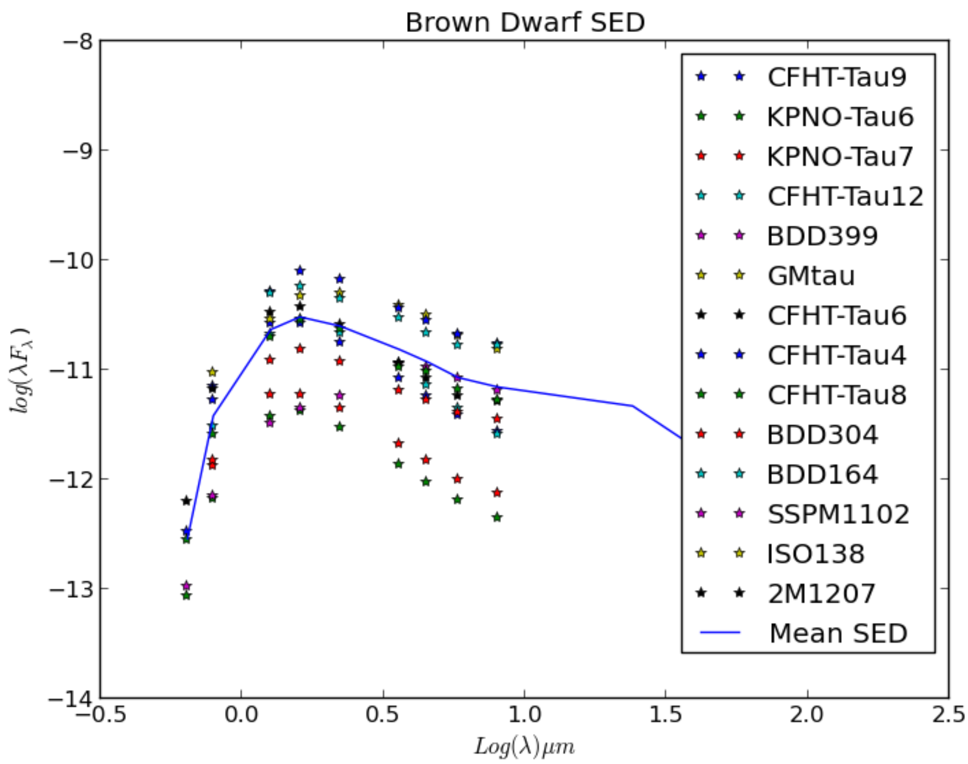

Figure 20: *Mean SED compiled from the individual photometric points of the Taurus brown dwarfs*

Object name	R	I	J	H	K	3.6μ	4.5μ	5.8μ	8.0μ	24μ	160μ (Jy)
CHFT-Tau 9	-	15.35	12.88	12.19	11.76	11.11	10.8	10.48	9.85	6.79	-
KPNO-Tau 6	20.56	17.9	15	14.2	13.69	13.08	12.77	12.41	11.82	9.1	-
KPNO-Tau 7	-	17.16	14.52	13.83	13.27	12.6	12.27	11.93	11.26	8.44	-
CHFT-Tau 12	-	16.26	13.15	12.15	11.55	10.77	10.54	10.31	9.93	8.25	-
BDD399	20.33	17.84	15.18	14.13	12.98	10.79	10.14	9.61	8.91	5.03	-
GMTau	-	15.04	12.8	11.59	10.63	9.44	8.95	8.64	7.97	5.33	-
CHFT-Tau 6	18.39	15.4	12.65	11.84	11.37	10.78	10.37	10.03	9.16	6.44	-
CHFT-Tau4	19.1	15.64	12.17	11.01	10.33	9.51	9.08	8.63	7.85	4.96	-
CHFT-Tau 8	19.27	16.43	13.19	12.12	11.45	10.85	10.23	9.86	9.14	6.53	-
BDD304	-	17.03	13.73	12.8	12.22	11.38	10.87	10.4	9.59	6.26	-
BDD164	-	-	12.2	11.36	10.76	9.75	9.34	8.87	7.89	4.3	-
SSPM1102	-	-	-	-	-	-	-	-	-	-	7.1e-3
ISO138	-	-	-	-	-	-	-	-	-	-	15e-3
2M1207	-	-	-	-	-	-	-	-	-	-	7e-3

Table 2: *Photometric observations of Taurus brown dwarfs with IR excess from Guieu et al. (2007) and Harvey et al. (2012). The flux values are represented in magnitudes except for 160μ which is represented in Jansky*

4.2 FITTING WITH BLACKBODY

The short wavelength part(R, I, J, H, K bands) of the mean brown dwarf SED was fitted with a black body to constrain the temperature and radius. For an initial comparison median SEDs of protoplanetary disks around T Tauri stars (Mathews et al., 2013) and a Herbig stars (Mulders & Dominik, 2012) were also fitted with stellar black bodies.
By fitting the stellar black bodies to the SEDs, the temperatures for the mean brown dwarf, median T-Tauri and median Herbig stars to be 2700K, 3700K and 8500K respectively. Since the brown dwarf candidates from Guieu et al. (2007) and T-Tauri candidates in Mathews et al. (2013) are from the Taurus star forming region the blackbodies are calculated for a distance of 140pc. Mulders & Dominik (2012) scaled their median Herbig SED to 140pc, given that their sample composed of Herbig stars from different star forming regions.

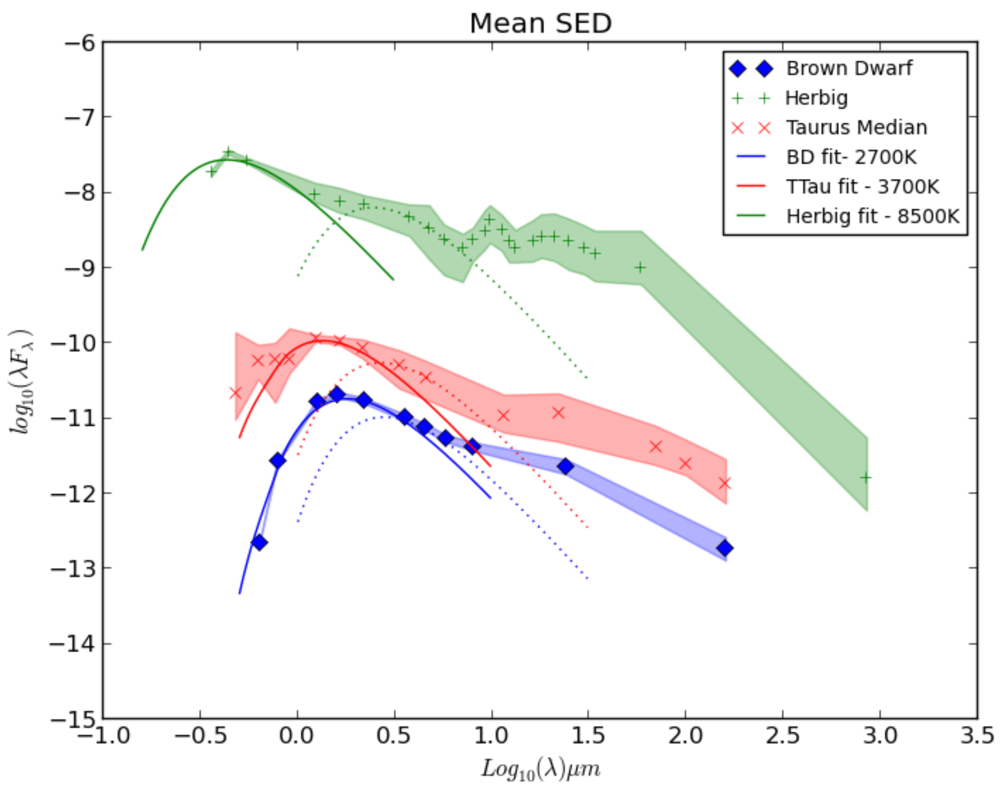

Figure 21: *Black body fit of mean brown dwarf, median T Tauri and median Herbig SED. The shaded region mark the upper and lower quartiles. The dotted curves are the black body fit for the inner regions of the disk*

We can also fit the infrared excess part of the SED with a blackbody (shown by dotted lines in fig.21). The black body curve for the disk can be calculated from eq.33 (Chiang & Goldreich, 1997).

$$4\pi d^2 \nu F_\nu = 8\pi^2 \nu \int_{R_{in}}^{R_{out}} da a B_\nu(T_e) \tag{33}$$

Where, d is the distance to the source, R_{in} and R_{out} are the inner and outer radius of the disk. $B_\nu(T_e)$ is the planck function and T_e is the effective temperature for the black body. This effective temperature depends on the part of IR excess that the blackbody fits. Fig.3 shows that the IR excess can have three domains,

- Wien domain

- Energetic domain
- Rayleigh-Jeans domain

The main portion of energy is emitted in a wavelength range which depends on the minimum and maximum temperatues of dust in the disk. This region is called the "energetic domain". The higher energy or smaller wavelength part is called as the "Wien domain" and the longer wavelength domain is called the "Rayleigh-Jeans" domain. Hence, the blackbody fit of the Wien domain will give us the highest temperature of dust in the disk. From the above blackbody fit in fig.21, the temperature is found to be about 1500K which is the dust condensation/sublimation temperature.

The effective temperature of the radiation emitted by the disk at a radius a is given by Chiang & Goldreich (1997),

$$T_e \approx \left(\frac{\alpha}{2}\right)^{1/4} \left(\frac{R_*}{r}\right)^{1/2} T_* \tag{34}$$

α is the angle at which the stellar radiation is incident on the disk, T_* and R_* is the effective temperature and radius of the star. The disk structure mainly affects in the energetic domain of the SED.

4.3 FITTING WITH PRODIMO

After the initial results from fitting the SED with a blackbody, I extended the SED fitting to a more detailed radiative transfer model ProDiMo. The working of ProDiMo is described in sect.1.5. I fitted the mean brown dwarf SED using parameterized ProDiMo models, where I specify the scale height and flaring manually without going through the hydrostatic structure step in the global iterations of ProDiMo.

All the ProDiMo models described in the sections that follow are parameterized over the vertical structure.

4.4 DEGENERACIES

The parameters that determine the SED of a protoplanetary disk are extremely degenerate. This is because every part of the SED is affected by more than one disk parameter. As mentioned in sect.4.2, the near and mid infrared (4.5 μm to 24 μm) part of the mean brown dwarf SED are affected mainly by the disk geometry. For example, the values for the power law index of the vertical column density (ϵ) and the flaring index (β) affect the mid-IR part of the SED as seen in fig.22. Hence, the emission in mid-IR can be explained by both ϵ and β. This makes it hard to determine the contribution of each of those parameters to the flux observed at those wavelengths. Thus the structure of a protoplanetary disk derived purely from SED is highly ambigous.

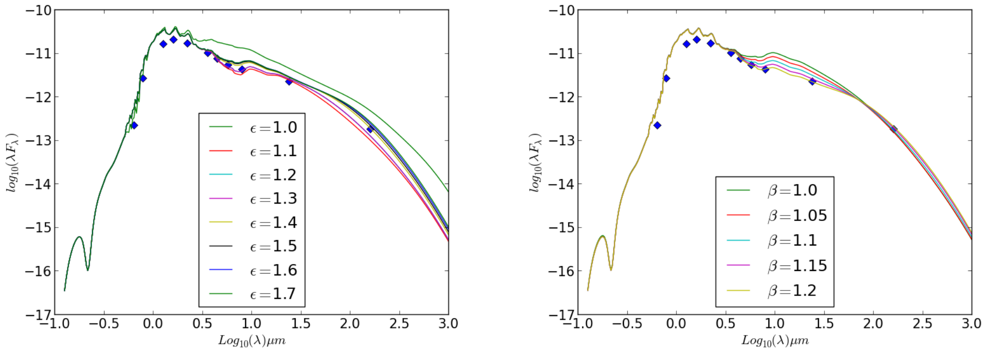

Figure 22: *ProDiMo models with different values of vertical coloumn density power index (ϵ) and flaring index (β).*

4.5 REDDENING

Another important factor to be considered when fitting an SED is the interstellar extinction. The extinction at small wavelegths is higher than that at longer wavelengths. Hence, the peak of the SED shifts towards longer wavelengths, i.e. the SED reddens. The blackbody or the modelled SED should be reddened in order to fit the source SED. (Cardelli et al. 1989) found a polynomial relation between the wave number and the extinction of the correspoding wavelength.
The extinctions for the selected sample of Taurus brown dwarfs were taken from Mayne et al. (2012). The value for A_v for the mean brown dwarf was chosen within the range of values given in Mayne et al. (2012) to get a better fit with the stellar blackbody on short wavelengths. The resultant extinction coefficient for the mean brown dwarf was found to be $A_V = 3.2$.

4.6 BEST FITTING PRODIMO MODEL

The mean brown dwarf SED was fitted manually from ProDiMo, using inital parameters such as effective temeperature, stellar luminosity, visual extinction coefficient(A_V) from the blackbody described in sect.4.2. The parameters for the best fitting model of the mean brown dwarf is given in table 3 and the best fit for the SED is shown in fig.23.

Table 3: *Best fitting mean brown dwarf parameters for ProDiMo*

Parameter	Description	value
M_*	Stellar Mass	0.078 $M_\odot$
L_*	Stellar Luminosity	0.025 $L_\odot$
T_{eff}	Stellar effective temperature	2700 K
M_{disk}	Disk mass	$1.10 \times 10^{-4} M_\odot$
R_{in}	Inner radius	0.0195 AU
R_{out}	Outer radius	200 AU
dust-gas	Dust to gas ratio	0.01
d	Distance	140 pc
incl	inclination	15°
H_0	scale height at a radius of 1 AU	0.125 AU
β	flaring index	1.1

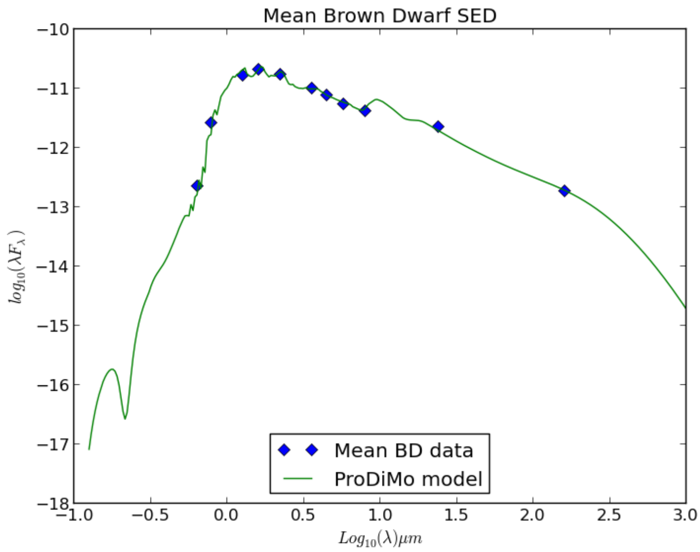

Figure 23: *Mean brown dwarf SED with best fitting ProDiMo model*

MEAN BROWN DWARF MODEL 5

5.1 INTRODUCTION

The brown dwarf formation process can affect the structure of the protoplanetary disks around them as described in sect.1.3.6. Hence, by measuring the radial and vertical structure of the protoplanetary disk around brown dwarfs, we can comment on their formation scenario. In this chapter, I will discuss the results of the best fitting mean brown dwarf ProDiMo model derived in sect.4.6 and make a relative comparison of the results with that of a standard T Tauri ProDiMO model described in sect.5.2 to study the differences in their chemical composition and thus comment on the formation of the brown dwarfs used to compile the mean brown dwarf SED and on the planet formation around them.

5.2 STANDARD T TAURI DISK MODEL

The mean brown dwarf protoplanetary disk ProDiMo model was compared with a standard T-Tauri disk model with the parameters given in Table 4

Table 4: *Parameters for standard T Tauri model in ProDiMo*

Parameter	Description	value
M_*	Stellar Mass	0.8 $M_\odot$
L_*	Stellar Luminosity	0.7 $L_\odot$
T_{eff}	Stellar effective temperature	4400 K
M_{disk}	Disk mass	0.01 $M_\odot$
R_{in}	Inner radius	0.1 AU
R_{out}	Outer radius	300 AU
dust-gas	Dust to gas ratio	0.01
d	Distance	140 pc
incl	inclination	45°
H_0	scale height at a radius of 1 AU	0.1 AU
β	flaring index	1.13

5.3 RADIAL STRUCTURE

The slope of the SED at long wavelengths (>24μm) is determined mainly by the disk mass and the outer radius. If we fix the disk mass from the relation derived by Mohanty et al. (2013) as $M_{disk} = (3.98 \times 10^{-3}) \times M_*$, then we get an extended outer radius ($\approx$ 200AU) as one of our solutions. Such large disks around brown dwarfs reveal large differences in the disk chemical structure compared to a typical T Tauri disk of that size.
Alexander & Armitage (2006) extended the mass accretion rate to stellar mass relation, i.e. $\dot{M}_{acc} \propto M_*^2$, to the low mass regime and found that, in order to maintain the relation in the low mass and substellar regime they have to assume an initial disk size of brown dwarfs to be larger than expected ($\approx 50 - 100$AU).
Ricci et al. (2012) measured an outer radius of 15-40AU for ρ oph 102, by imaging the disk in

continuum using ALMA. However, this outer radius is only a measure of the radial extent in dust. Hughes et al. (2008) and Andrews et al. (2012) found from SMA observations of T Tauri and Herbig disks that the outer radius of gas traced by CO sub-mm lines is larger than that of dust. This can be explained by assuming a tapered edge and an exponential surface density cut off in the disk. Pinilla et al. (2013), also explained that the dust grains can move radially inwards in brown dwarf disks more efficiently than in T Tauri disks. This explains the smaller outer radii in dust which were previously measured around brown dwarfs (Ricci et al., 2012).
Detecting such radially extended disks can hint to the possible formation mechanism for those brown dwarfs. As explained in sect.1.3.6, brown dwarfs which formed due to dynamical ejection or photo-erosion cannot host extended disks. In the case of the ejection scenario, the dynamical time scale of the disk is large compared to the timescale in which the object is ejected out of the star forming region. In the case of photo-erosion, the circumstellar material is lost to the ionization front and hence there is less material that surrounds the disk. However, if the brown dwarf is formed by gravitational or turbulent fragmentation it can host a larger disk.
Recent sink particle hydrodynamical simulation with radiative transfer by Bate (2012) on brown dwarf formation found that 50% of the brown dwarfs have an outer radius smaller than 10AU, 20% have an outer radius larger than 40AU and $\leqslant$10% have an outer radius larger than 100AU. Ricci et al. (2014) observed three taurus brown dwarfs (CHFT-Tau 4, 2M0444 and CIDA 1) with ALMA in the continuum (Band 3/ 93GHz and Band 7/ 338GHz). They find that the disks around these brown dwarfs are extended having outer radii >80AU, 139AU and 66AU respectively.

5.4 PHOTOCHEMISTRY

For a protoplanetary disk around a brown dwarf with a disk mass of about $10^{-6}M_{\odot} - 10^{-3}M_{\odot}$ [(Harvey et al., 2012),(Mohanty et al., 2013)] and assuming a canonical dust to gas ratio of 0.01, the total dust mass is quite low for the disk. This makes an extended disk ($\sim 80 - 200$AU) optically thin at UV and Optical wavelengths of the wavelengths. Hence, radiation dominates the chemistry in these disks driving more photochemical reactions such as photodesorption, photoionization, etc. fig.24, shows the distribution of water in the mean brown dwarf disk and a standard T Tauri disk.

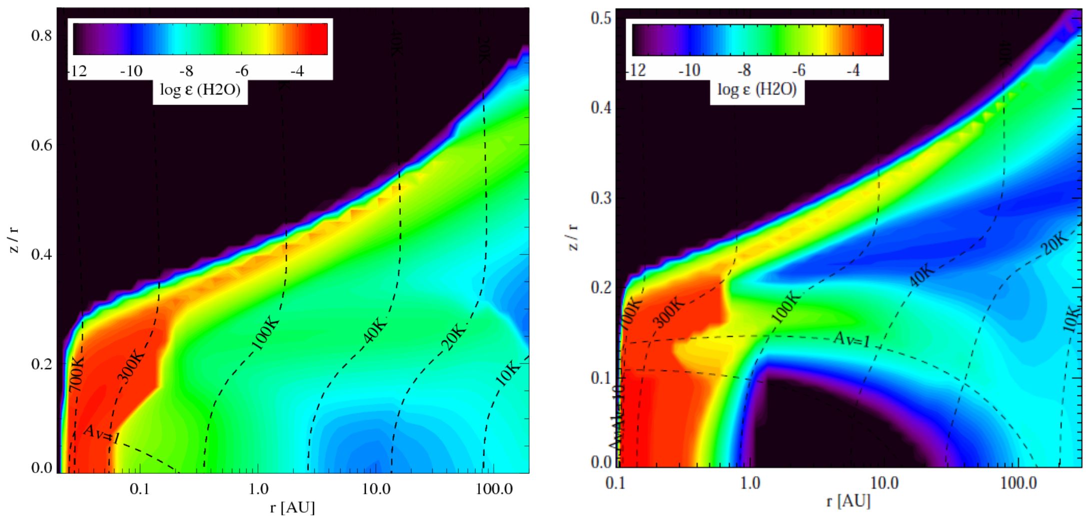

(a) *Mean brown dwarf disk*

(b) *Standard T Tauri disk*

Figure 24: *Abundance distribution of water in the protoplanetary disk over plotted with dust temperatures and* $A_V = 1, 10$ *contours*

In fig.24, we can see that water still exists in the gas phase in the mean brown dwarf model even at extremely low temperatures down to the midplane of the disk. This is due to highly efficient photodesorption of ice from dust grains in the mean brown dwarf disk. When an incident UV photon hits an ice mantle around a dust grain, it ejects a water molecule back to the gas phase. This extends the snow-lines in these disks and thus affects planet formation around them. This ice line extension can also be seen in CO and HCO+.

The position of the snowline affects the formation of planets in the disk. If the snowline is extended as seen in the mean brown dwarf model, the probability of forming ice giants like uranus or neptune is lower as there is lesser amount of grains inside the snowline to form planetary embryos.

5.5 COMPARISON WITH OBSERVATIONS

A parameterized ProDiMo model of 2M0444 was built using the stellar and disk parameters derived by Ricci et al. (2014) given in Table 5.

Table 5: *Parameters for 2M0444 from Ricci et al. (2014)*

Parameter	Description	value
M_*	Stellar Mass	0.05 $M_\odot$
L_*	Stellar Luminosity	0.028 $L_\odot$
T_{eff}	Stellar effective temperature	2838 K
M_{disk}	Disk mass	$1.99 \times 10^{-4} M_\odot$
R_{in}	Inner radius	0.05 AU
R_{out}	Outer radius	139 AU
dust-gas	Dust to gas ratio	0.01
d	Distance	140 pc
incl	inclination	30°

When compared to the mean brown dwarf model, the 2M0444 model has strong signs of photochemistry and extended icelines as seen in fig.25.

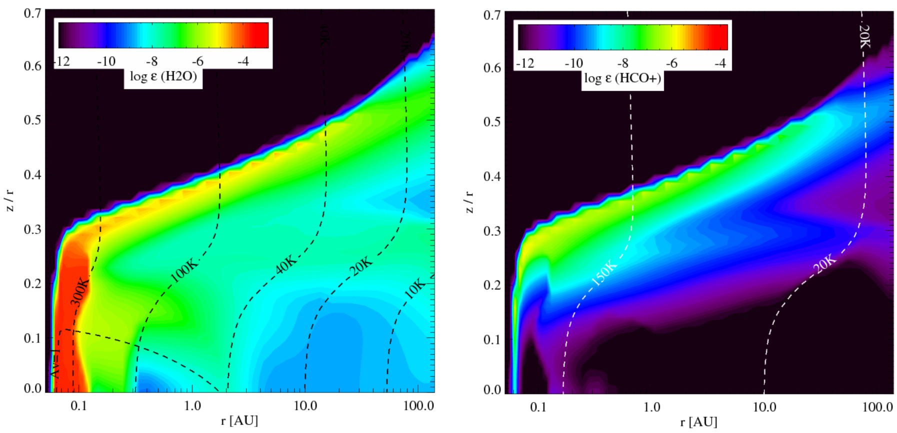

(a) H_2O (b) *HCO+*

Figure 25: *abundance distributio of water and HCO+ in the 2M0444 disk ProDiMo model over plotted with dust temperature and visual extinction contours*

5.6 PROPOSED OBSERVATIONS

Following up on Ricci et al. (2014) ALMA cycle 0 observations and based on the results from the mean brown dwarf ProDiMo model, we can measure the radial extent of the disks around the Taurus brown dwarfs and also measure the extent of their icelines (CO & H_2O).
The sub-mm lines are well suited for measuring the structure of protoplanetary disks. The disks are mostly optically thin in the continuum down to the midplane for sub-mm lines. Hence, these lines are the most efficient probe to observe the disk all the way to its midplane. The dashed line contours in the bottom panel of fig.26 shows the region from where the CO(2-1) line is emitted.

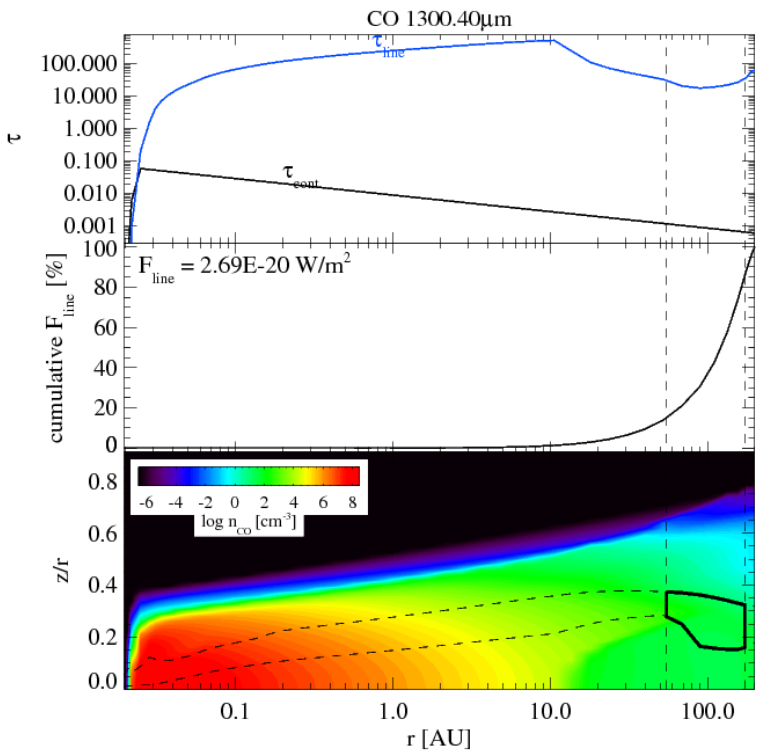

Figure 26: *emission of CO(2-1) line in the mean brown dwarf model as a function of distance from the central object. The top panel shows the optical depth of the line and the continuum. The midpanel shows the cumulative line flux. The bottom panel shows the radial and vertical regions from where the line is emitted where the solid box shows the region in the disk where the cumulative line flux is above 15%.*

The radial extent of the disk as mentioned before in sect.5.3, can vary for dust and gas. To measure the radial extent in dust, we can use the sub-mm continuum images and for the gas we can meausre it using the rotational lines of CO and its isotopes, as CO is the most abundant molecular species in the protoplanetary disk and it is emitted all the way out to the outer radius of the disk (fig.26.

The CO(2-1) line is the preferred rotational line in the sub-mm to measure the radial extent of the gas as it requires the lowest energy to be excited. Different isotopes of CO like ^{13}CO and $C^{18}O$ can be used to probe the disk at different scale heights. However, CO(1-0) line is not prefered for measuring the radial extent of the disk even though they have extremely low excitation energy, as the CO(1-0) line is mostly in the optically thick regime and since it requires extremely low energy for activation, it is extremely faint for most of the sources.

Ricci et al. (2014) observed CHFT-Tau4, 2M0444 and CIDA1 in both sub-mm continuum and CO(3-2) line in ALMA cycle 0 at baselines up to $\approx 400\mathrm{m}$. However, he did not detect the CO(3-2) line in CHFT-Tau 4 during ALMA cycle 0 due to its limited sensitivity. With the high sensitivity of present day configurations of ALMA and its high spatial and spectral resolution, we can now measure the outer radius more accurately and resolve the difference between gas and dust outer radius.

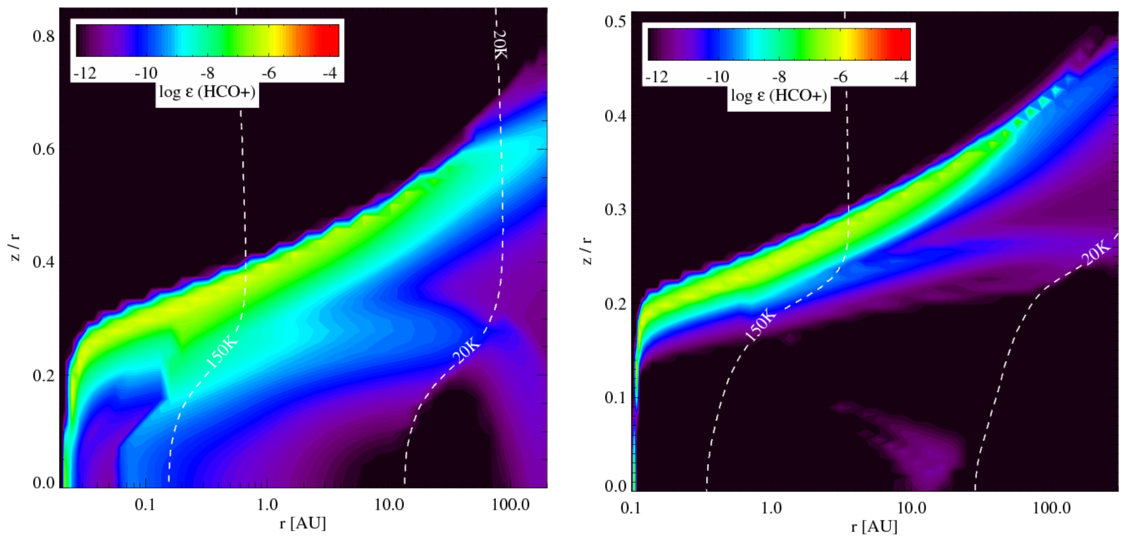

(a) *Mean brown dwarf* (b) *Standard T Tauri*

Figure 27: *Abundance distribution of HCO+ in the mean brown dwarf and standard T Tauri ProDiMo models, overplotted with the dust temperature contours of 150K and 20K*

Furthermore, we can probe into the photochemistry in the disk using tracers of snowlines such as DCO+ (4-3) and HCO+ (4-3). DCO+ (4-3) line traces the CO-iceline in the disk, as its formation reaction through H_2D+ requires a balance between low temperatures and gas phase abundance CO. Hence the emission of DCO+ will be an annulus around the CO snow line as it is enhanced near the 20K isotherm in the disk which is the CO iceline. HCO+ can be used to detect both photodesorption and photoionisation in the disk. HCO+ can also be used to measure the ionization fraction in the protoplanetary disk by measuring the line ratios of [DCO+]/[HCO+] in these disks. The ionization fraction can be used to constrain the Magneto Rotational Instability (MRI) with which we can contrain the lifetime of the disk and thus its planet formation time scales.

In the sections that follow, we shall discuss how ALMA in cycle 2 can be used to verify the results of the mean brown dwarf model. Also reproducing Ricci et al. (2014) CO (3-2) image through ALMA cycle 0 extended configuration, thus testing the ProDiMo 2M0444 model.

5.7 CASA

CASA or Common Astronomy Software Applications (McMullin et al., 2007) is a python based radio interferrometry data reduction tool specifically developed for ALMA and Extended Very Large Array (eVLA).CASA can also simulate observations for ALMA, eVLA and other radio interferrometers for a given skymodel.Simulations for ALMA observations were done using the functions simobserve and simanalyze in CASA. The simobserve task generates visibilities by observing the input sky-model through the given antenna configuration of ALMA for the given integration time. The simanalyze task analyzes the visibilties generated from simobserve and produces the synthesized image of the observed object.

5.8 SIMULATING ALMA OBSERVATIONS WITH PRODIMO

To simulate ALMA observation with CASA we need to generate a sky model from the ProDiMo disk model. This can be done by running ProDiMo with 2D line radiative transfer. ProDiMo uses a modified version of the Monte Carlo radiative transfer code RATRAN (Hogerheijde & van der Tak, 2000) to solve the 2D line radiative transfer described in Kamp et al. (2010). The output of the 2D line radiative transfer is in 3D data cube (2D grid of ProDiMo (r,z) + velocity in the third dimension) of line fluxes. The output line cube can be integrated over the velocities (-10 km/s to 10 km/s for the mean brown dwarf model) and regrided into the world coordinate system (WCS) by interpolating with the central objects position in WCS. The CO(2-1) skymodel for the mean brown dwarf disk ProDiMo model is shown in fig.28

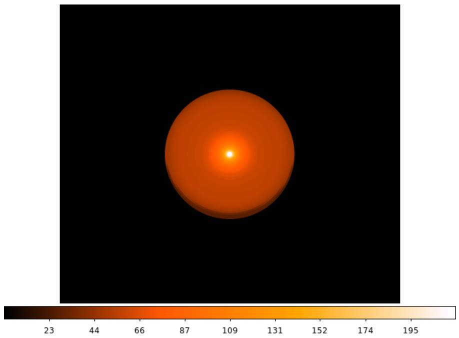

Figure 28: *CO (2-1) skymodel input for CASA of the mean brown dwarf ProDiMo model*

5.9 INPUTS FOR CASA

The integration time to observe the mean brown dwarf model in CASA was calculated using the ALMA observing tool for a spectral resolution and bandwidths of 122.07 kHz (0.2 km/s) and 234.4 MHz respectively for the CO(2-1) line and 244.14 kHz (0.2 km/s) and 468.8 MHz (394 km/s) for the HCO+ (4-3) line. The integration time for observations and its corresponding signal-to-noise ratios are given in table 6.

Table 6: *Integration time and S/N*

Line	wavelength/frequency	Integration time	S/N
CO(2-1)	1300.4µm/ 230.538 GHz	774.2 seconds	line (30mJy): 3.0
			continuum (0.35mJy): 1.5
HCO+ (4-3)	840.38µm/ 356.734 GHz	1306.4 seconds	line (50mJy): 5.0
			continuum (1.0mJy): 4.4

To measure the radial extent of gas in the disk through CO(2-1) line, it is essential to image the disk at the highest possible spatial resolution. ALMA in cycle 2 delivers a maximum spatial resolution of 0.18" for baselines extending up to 1.5 km. To probe the HCO+ line all the way till the cold regions of the disk, the sensitivity of the instruments should also be considered along with the spatial resolution. Hence, we chose a spatial resolution of 0.5". Assuming an extended disk of about 1-2" in diameter, we can resolve the disk at least with two to resolution elements radially. This observation was proposed in the ALMA cycle to given in appendix i as a pilot study which can be later followed up with new instruments of higher sensitivity and resolution.

Fig.29 and fig.30 are the simulated synthesis images of ALMA cycle 2 observations of the mean brown dwarf ProDiMo model. Fig.29a and fig.30a shows the simulated UV coverages, i.e. the antenna spacings and positions during the observation where U and V are the direction cosines at the position of the antenna with the Hour angle and declination of the phase center of the field. Fig.29b and fig.30b, shows the simulated Point Spread Functions (PSF) of the array. The point spread function is the response of the interferomter array to a point source. The observed images from any telescope is convolved with the point spread function and it is called the "Dirty Image". Fig.29c and fig.30c are the final images deconvolved from its PSF. Fig.29c and fig.30c also shows the contours of different flux levels till the level of the background noise. The system temperature which accounts for the thermal noise in the images are automatically chosen by CASA for predetermined water vapour levels in the atmosphere.

The outer radius of the disks cannot be constrained with only the synthesis image, as the line flux can exist even below the background noise level. Hence, to estimate the outer radius from sub-mm observations, we should also fit the observed visibilities along with the images.

CO(2-1)

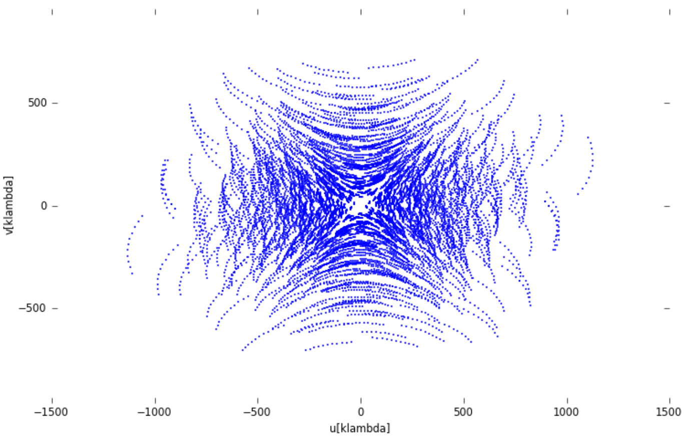

(a) *Simulated UV coverage*

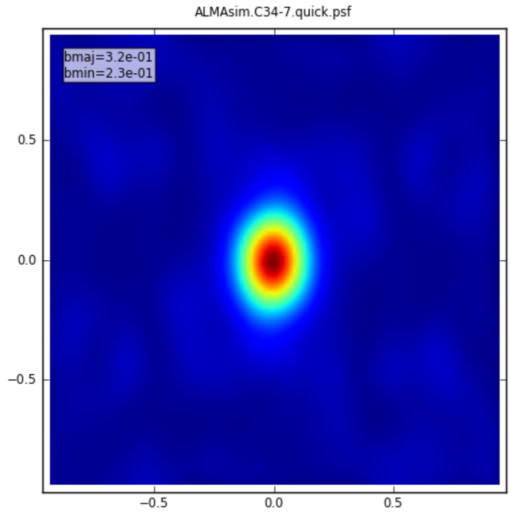

(b) *Simulated PSF*

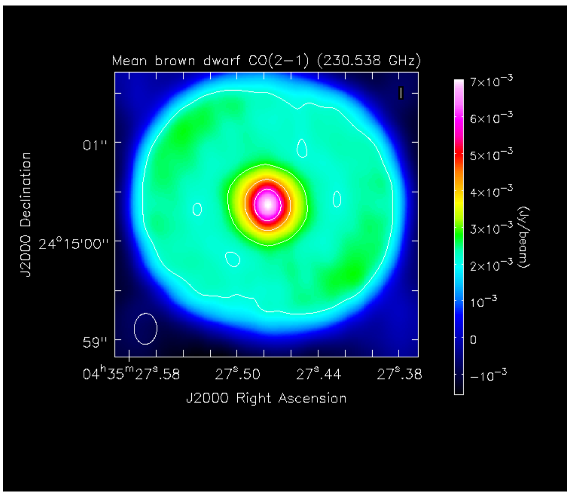

(c) *Synthesized image*

Figure 29: Simulated CO (2-1) observation of the mean brown dwarf model through the extended configuration of ALMA in cycle 2. The flux contour levels of 0.3, 0.4, 0.6 and 0.8 overplotted on the image

HCO+(4-3)

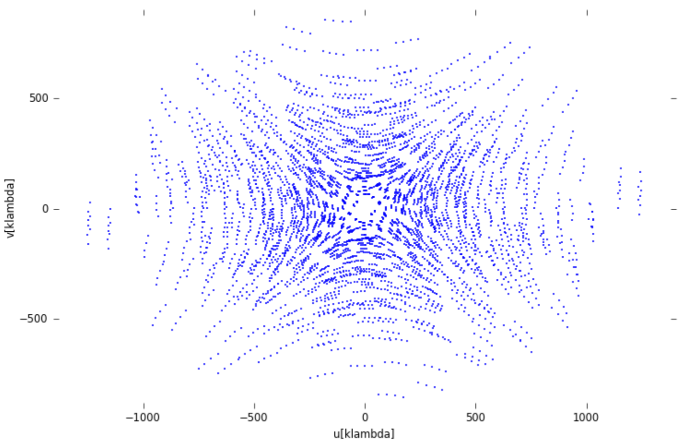

(a) *Simulated UV coverage*

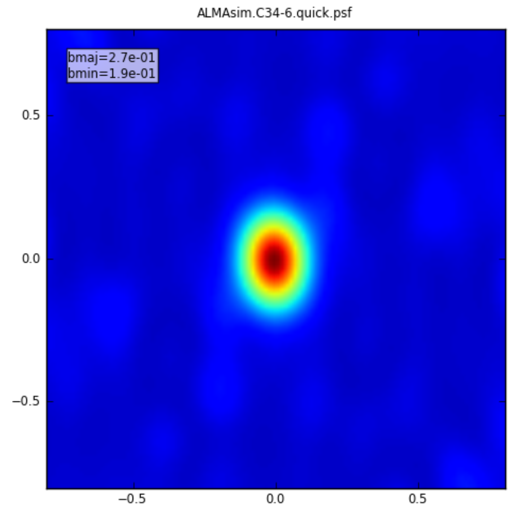

(b) *Simulated PSF*

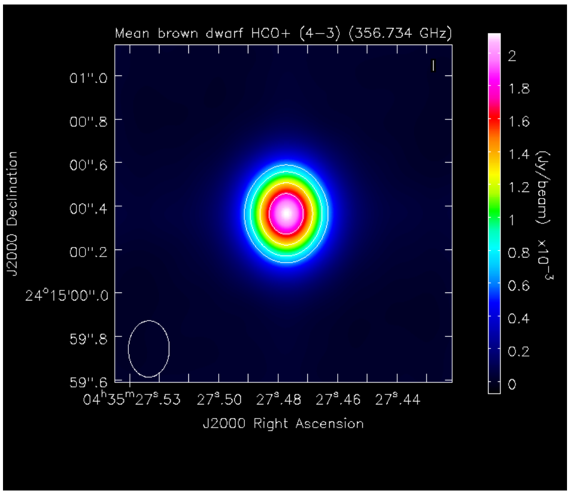

(c) *Synthesized image*

Figure 30: Simulated HCO+ (4-3) observation of the mean brown dwarf model through ALMA cycle 2. Flux contour levels of 0.3, 0.4, 0.6, 0.8 are over plotted on the image

The observations mentioned in above section were proposed as an observation in ALMA cycle 2 to measure the radial extent around 12 brown dwarf protoplanetary disks and detect photochemistry in two brown dwarf protoplanetary disks in the Taurus star forming region. A copy of the proposal is attached in Appendix i

5.10 2M0444

As a test for the 2M0444 ProDiMo model discussed in sect.5.5, the CO(3-2) line image of Ricci et al. (2014) was reproduced in CASA from the ProDiMo 2M0444 model. The array configuration was chosen as the extended configuration of ALMA cycle 0 with baselines extending upto 400 meters. The resulting simulated synthesis image with the actual observation is shown in fig.31.

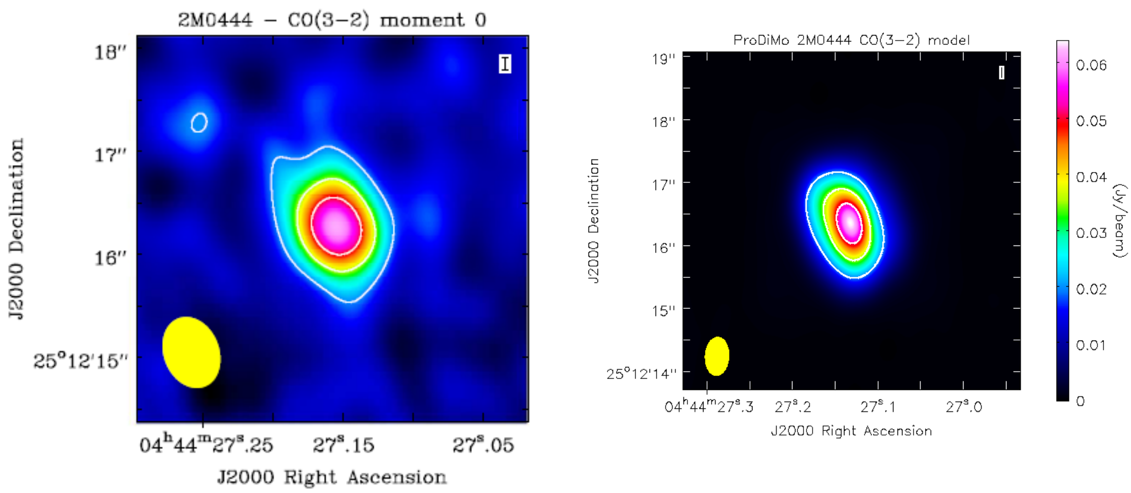

(a) *Ricci et al. (2014)* (b) *ProDiMo model*

Figure 31: *CO (3-2) line images of 2M0444 of Ricci et al. (2014) ALMA cycle 0 observations and simulated observation of ProDiMo model through CASA. Flux contour levels of 0.3, 0.55 and 0.8 are overplotted on the simulated image*

The resulting flux value for the continuum is 2.2mJy and for the CO(3-2) line is 4.155 Jy.km/s. However, Ricci et al. (2014) measured a continuum flux of 9.0 mJy in ALMA band 7 at 338GHz and a CO(3-2) line flux of 0.98 ± 0.03 Jy.km/s. The differences in the line and the continuum fluxes can be due to different types of dust grains assumed in the models by Ricci et al. (2014) and in our ProDiMo model. This affects the opacities of the model and thus the sub-mm flux.

The synthesized image by simulating ALMA observations of ProDiMo 2M0444 model shown in fig.31b, is similar to the actual observation of Ricci et al. (2014) shown in fig.31a. However, the assymetries in the disk cannot be captured in the simulation as the ProDiMo model is axisymmetric about the rotation axis of the disk.

6 CONCLUSIONS AND DISCUSSION

In this thesis, we hypothesize that a significant number of protoplanetary disks found around brown dwarfs have a scaled down structure of T Tauri and Herbigs. This scaling can be captured through simple analytic models described in Chapter 2. These analytic scalings are also consistent with detailed numerical models (ProDiMo) including 2D continuum radiative transfer and gas heating/cooling balance. By calibrating the analytic models to the structure of disks around T Tauri observed by Andrews & Williams (2007), the analytic models predict significantly smaller disks around brown dwarfs with outer radii of about 20-40AU. Also, as the surface density distribution of dust in the disk and the vertical structure of the protoplanetary disk depends on the stellar gravity and thus the mass of the central object, we can expect a first order scaling over stellar mass for these quantities.

Fitting the mean SED of 14 Taurus brown dwarfs, we find that extended disks ($\sim 200\text{AU}$) are still a possibility as degeneracies in SED fitting prevents us from deriving R_out from the SED alone. Alexander & Armitage (2006) show that to maintain scaling over the mass accretion rate in brown dwarfs ($\dot{M}_{acc} \propto M_*^2$), they need the disks around brown dwarfs to be radially extended ($\approx 50-100\text{AU}$). For a total dust mass $\sim 10^{-6} M_\odot$ in such an extended disk, will result in highly optically thin regions and hence photochemistry will dominate in these disks.

The radial extent of the brown dwarf protoplanetary disk depends on the formation path of its central object. To host an extended protoplanetary disk, the central brown dwarf cannot be formed through the ejection or the photo-erosion scenarios, as they strip away material from the disk. Hence, gravitational fragmentation, turbulent fragmentation and gravitational instability models can potentially be their formation paths.

Planet formation around brown dwarfs is affected by the structure of the disk. If the snowlines are extended in the brown dwarf disks, the probability of forming ice and gas giants are significantly low as there is less amount of mass in solids to form sufficiently large planetary embryos within the snowline. Also, if the disk is strongly affected by photoionization, then the ionization fraction drives the MRI in the disk increasing the turbulence. This strongly affects the lifetime of the disks around brown dwarfs and thus the planet forming timescales.

Ricci et al. (2012) measured an outer radius of $\approx 20-40\text{AU}$ from their ALMA observations of ρ-Oph 102. This agrees with the outer radius of the brown dwarf protoplanetary disk predicted by the analytic models. However, Ricci et al. (2014) also observed radially extended disks around three brown dwarfs (2M0444, CHFT-Tau 4 and CIDA 1) in the Taurus star forming region. This agrees with the results of the mean brown dwarf ProDiMo model described in Chapter 5. Hence, we can conclude that even though most of the brown dwarf protoplanetary disks could be scaled down versions of T Tauri and Herbigs, some of the disks around brown dwarfs can be more radially extended and thus have different chemical processes dominating in them.

FUTURE WORK

Probing the structure and chemistry of brown dwarf protoplanetary disk is made possible with the arrival of new telescopes with cutting edge technologies like ALMA, SKA, eELT, etc. which offer high sensitivity and high spatial and spectral resolution. Also, recent developments in detailed radiative transfer, hydrodynamic and chemical model codes have made the protoplanetary disk models more robust in reproducing the physical and chemical processes in them.

With better spatial and spectral resolution of ALMA's full operation mode, we can follow up previous observations of brown dwarf protoplanetary disks in the Ophiuchus and Taurus star forming regions ((Ricci et al., 2012), (Ricci et al., 2014)) through sub-mm molecular lines and continuum observations to resolve the radial structure of the brown dwarf protoplanetary disks to a greater detail, measure the extent of CO ice these disks through DCO+ line to compare the efficiency of planet formation between an extended and a compact disk, and estimate the ionization fraction through HCO+ line and thus constrain the disk life time and estimate their accretion rates.

Following up on the results of Bate (2012) SPH simulations, we can adapt a mesh refinement in their simulation to probe more into the effects of different formation scenarios on the disk structure. Additionally, we can also investigate the effects on the brown dwarf disk structure during its evolution.

ACKNOWLEDGMENTS

First, I would like to thank my supervisor Prof. Inga Kamp for all her motivation and support throughout the entire period of the project. She motivated me during all our weekly meetings and was enthusiastic about all the results and ideas that I discuss with her, regardless of its importance to the final goal of this project. She was available anytime to solve my problems and explain all the concepts in detail. Secondly, I would like to thank my Parents and my sister Anusha Muthusubramanian for supporting me with all their love. I would also like to thank Stefano Antonellini for all the discussions we had during this work and helping me out with all my difficulties with ProDiMo and also for giving me some tips and tricks with the code. Also I would like to extend a special thanks to Robin Kooistra for his friendship and useful discussions about both of our work which helped me a lot throughout this work. I would also like to thank the entire disk group for their useful discussions during our group meetings. I also thank Peter Woitke, Wing-Fai Thi, Francois Menard from the DIANA team for helping me out with all their useful discussions during my ALMA proposal and also during the later stages of this project. Last but not the least, I would like to thank everyone in the office 134 at Kapteyn Institute for giving me the perfect dutch experience and supporting me throughout my stay at Kapteyn institute as a masters student.

Part I

APPENDIX

INGA KAMP 2013.1.00928.S

PROJECT TITLE:	Constraining the disk lifetime in brown dwarfs				
PRINCIPAL INVESTIGATOR NAME:	Inga Kamp	PROJECT CODE:	2013.1.00928.S		
SCIENCE CATEGORY:	Circumstellar disks, exoplanets and the solar system	ESTIMATED 12M TIME:	7.4 h	ESTIMATED ACA TIME:	0.0 h
CO-PI NAME(S): (Large Proposals only)					
CO-INVESTIGATOR NAME(S):	Balaji Muthusubramanian; Francois Menard; Peter Woitke; Wing-Fai Thi				

EXECUTIVE SHARES[%]:	NA : EU : EA : CL : OTHER :	0 100 0 0 0	STUDENT PROJECT? (Yes/No)	Yes
			RESUBMISSION? (Yes/No)	No

ABSTRACT

Brown dwarfs have a formation process similar to that of low mass stars. Even though brown dwarfs may not burn hydrogen in their cores, they do posess disks with gas and dust around them where planets can form. With the high spatial resolution and sensitivity of ALMA cycle 2 observations, we propose to measure for the first time, the spatial extent of the gas and dust in a sample of 12 brown dwarf disks in Taurus. The three brightest targets from the sample are chosen for a pilot study to detect the HCO+ line and thus determine the ionisation degree in the disk and the presence of photochemistry. The results have strong implications for the nature of planets that can form around brown dwarfs.

REPRESENTATIVE SCIENCE GOALS (UP TO FIRST 5)

SCIENCE GOAL	POSITION	FREQUENCY	BAND	ANG.RES.(")	ACA?
Measurement of extent of gas in the disk	J2000: 04:24:26.4600, 26:49:50.300	230.53800 GHz	6	0.2	N
Detection of Photochemistry in the disk	J2000: 04:39:03.9600, 25:44:24.400	356.73424 GHz	7	0.5	N
Total # Science Goals : 2					

SCHEDULING TIME CONSTRAINTS (e.g. Co-ordinated observations already scheduled)	NONE	Time estimates overridden?	No

PI CONTACT INFORMATION

INSTITUTE &/OR DEPT.	Kapteyn Astronomical Institute, University of Groningen		
TITLE : NAME : E-MAIL : PHONE[FIRST] : PHONE[SECOND] : FAX :	Inga Kamp kamp@astro.rug.nl	ALMA EXECUTIVE : ADDRESS :	EU

Constraining the disk lifetime of Brown Dwarfs

PI: Inga Kamp

Abstract

Brown dwarfs have a formation process similar to that of low mass stars. Even though brown dwarfs may not burn hydrogen in their cores, they do posess disks with gas and dust around them where planets can form. With the high spatial resolution and sensitivity of ALMA cycle 2 observations, we propose to measure for the first time, the spatial extent of the gas and dust in a sample of 12 brown dwarf disks in Taurus. The three brightest targets from the sample are chosen for a pilot study to detect the HCO+ line and thus determine the ionisation degree in the disk and the presence of photochemistry. The results have strong implications for the nature of planets that can form around brown dwarfs.

1 Scientific Justification

1.1 Introduction

Brown dwarfs have masses between that of a star and a planet. However, they also process gas and dust around them to form protoplanetary disks. The two main models for the formation of brown dwarfs are core fragmentation, where a dense core fragments to lower mass cores due to turbulence (Padoan & Nordlund, 2002) and the ejection model, where the protostars that grow in a cluster, get ejected before they have time to grow beyond 0.075 $M_{\odot}$ (Reipurth & Clarke, 2001). These models are not mutually exclusive and can infact co-exist. Alexander & Armitage (2006) argue that brown dwarf protoplanetary disks initially have larger radii and smaller accretion rates ($10^{-8} \sim 10^{-12} M_{\odot}/year$) than that of the higher mass stellar counterparts, resulting in longer disk lifetimes. Also, turbulence in the disk forming due to Magneto-Roatational Instability (MRI), can affect the disk's accretion rate. The ejection model cannot support large disks as the other massive stars in its neighborhood will strip material from their outer disks. Hence, measuring the sizes of disks around a larger sample of brown dwarfs will throw light on their formation process and determine their chemical composition.

Systematic studies on brown dwarf disks are now feasible with the arrival of multi-wavelength studies with increased senstivity on telescopes like Herschel, VLT, SMA and ALMA. Also, high computing power and more detailed radiative transfer and thermo-chemical models have broadened our knowledge on brown dwarf disks. We propose to observe the disks around 12 Taurus brown dwarfs to measure the gas and dust radial sizes of a representative sample of disks through 12CO 2-1 line and contiuum measurements. In addition, we aim to detect turbulence and also estimate the position of snowline through deep observation of the HCO+ 4-3 line for the 3 brightest targets, in which one of them is already resolved both in continuum and 12CO in cycle 0 (Ricci et al., 2013).

1.2 Disk Models

We compiled a mean SED from the photometric data of brown dwarfs with IR excess from Guieu et al. (2007) and 70 μm and 160 μm data from Harvey et al. (2012) and used the thermo-chemical code ProDiMo (Woitke et al., 2009) to study the physical and chemical properties in such a mean BD disk. Our disk models with a large outer radius of $\sim$ 200AU reveal large differences in disk chemical structure compared to a typical T Tauri disk of that size.

Pinilla et al. (2013) found from ALMA cycle 0 observations of ρ oph 102 (Ricci et al., 2013) that millimeter sized grains are only extended out to 15-40AU, much less than the outer radius we used in our models. Hughes et al. (2008) and Andrews et al. (2012) found from SMA observations of T Tauri and Herbig disks that the outer radius of gas traced by CO sub-mm lines is larger than that of dust. It can be explained with a tapered edge and an exponential surface density cut off. However, the dust grains according to Pinilla et al. (2013) can efficiently move radially inwards in brown dwarfs when compared to T Tauri disks, which accounts for smaller outer radii seen in the sub-mm size dust distribution. The larger mm-sized dust grains would then decouple more easily from the gas and show larger discrepancies with respect to the gas measurements than that of smaller grains.

The disk parameters we used in our ProDiMo model are given in Table 1 and the resulting mean SED is shown in Figure 1c. It is clear that an SED alone cannot be used to measure disk outer radii. Hence, we need ALMA to image these disks both in continuum and the lines.

1.2.1 Disk Chemistry as a diagnostic for Planet Formation

Harvey et al. (2012) show from Herschel observations that the disk mass for brown dwarfs is in the range $10^{-6}M_{\odot} \sim 10^{-3}M_{\odot}$, which is a lower disk to stellar mass ratio than for T Tauri disks. Assuming a canonical dust to gas ratio of 0.01, the total dust mass is quite low for a large disk, making the disk more optically thin at most wavelengths. Hence, photochemistry could dominate almost down to midplane in these disks, implying that the water and CO snowlines should be much further out than compared to what is estimated from the dust temperature. Figure 1a and Figure 1b show the distribution of HCO+ in the brown dwarf model and in a T Tauri model. We can conclude that HCO+ is more abundant in the gas phase around the mid plane of the brown dwarf disk than in the T Tauri disk. This is due to efficient photodesorption of ices in brown dwarf disk model. From the HCO+ emission, we can measure the ionisation fraction in these disks which will be a measure for the MRI in these disks and thus a pointer for turbulence in the disk. This would strongly affect the lifetimes of these disks and hence the planet formation process in these brown dwarf disks.

1.3 Goals for the proposed observation

Our sample contains 12 brown dwarfs in Taurus selected from the samples with IR excess in Guieu et al. (2007), which was also used in our mean SED fitting in §1.2 and 2MASS 0444+2512 from Ricci et al. (2013). The CO 2-1 line of ρ oph 102 and 2MASS 0444+2512 has been detected in cycle 0 (Ricci et al., 2013) and the flux of ρ oph 102 is 530mJy. The continuum flux of both objects at 850 μm is 4.1mJy and 9.85mJy respectively (Ricci et al., 2012) (Mohanty et al., 2013).

Our **first Science goal** is to measure the brown dwarf disk's radial extent of dust and gas with the continuum at 230GHz and the CO 2-1 line. In band 6 of ALMA cycle 2, we go for an angular resultion of 0.18", which corresponds to the largest baseline of 1.5 km. At this angular resolution, we will resolve the disk down to 10-20 AU, which is sufficient to distinguish between large ($\sim$ 100AU) disks and small disks ($\sim$ 40AU). In 4.8hours, we will achieve the required continuum sensitivity of 0.3mJy in 13mins per source pointing and a line sensitivity of 30mJy. We resolve the lines with 5 resolution elements if they are as narrow as 1 km/s.

The second goal is to detect the HCO+ 4-3 line in the three brightest brown dwarf disks. From the HCO+ we can determine the ionisation fraction through the CO/HCO+ ratio and thus detect the presence of turbulence. We might also detect gas phase emissions of HCO+ around mid plane of these disks which will be a strong pointer for photochemistry in these disks. For a sample of T Tauri disks Öberg et al. (2011) found typical CO 2-1 to HCO+ 3-2 line ratios of $\sim$ 3-10. Based on the previous CO detection of ρ oph 102, we expect an HCO+ line flux of 50mJy. For 22 minutes on source, we reach a line sensitivity limit of 10mJy.

2 Potential for Publicity

Our ALMA observations will measure for the first time the sizes of a representative sample of Taurus brown dwarfs disks. The sizes of the disk have direct implications for the disk lifetime, hence the timescale for dust grain growth and eventually planet formation. If ALMA detects the HCO+ gas emission in the cold regions of the brown dwarf disk, we can constrain the amount of turbulence in the disk and thus put additional constrains the timescale available for planet formaiton.

3 Figures and Tables

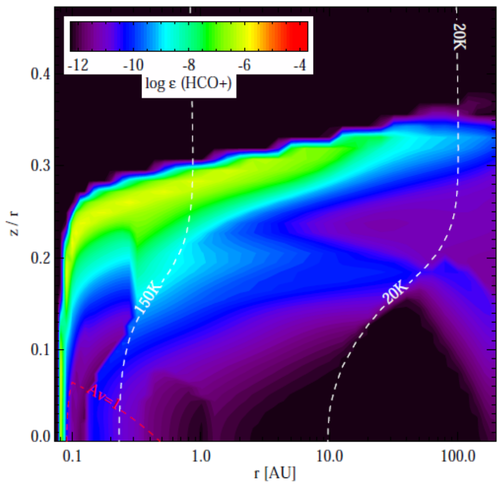

(a)

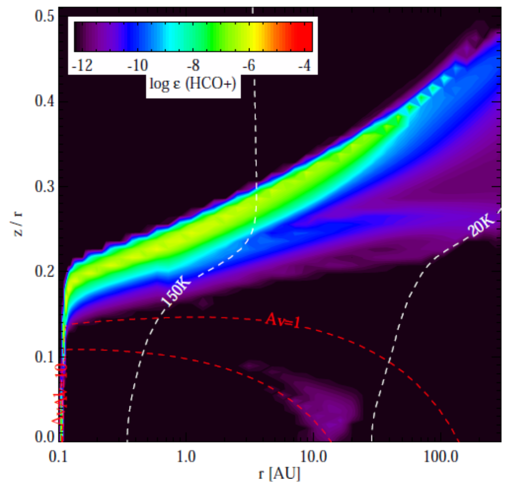

(b)

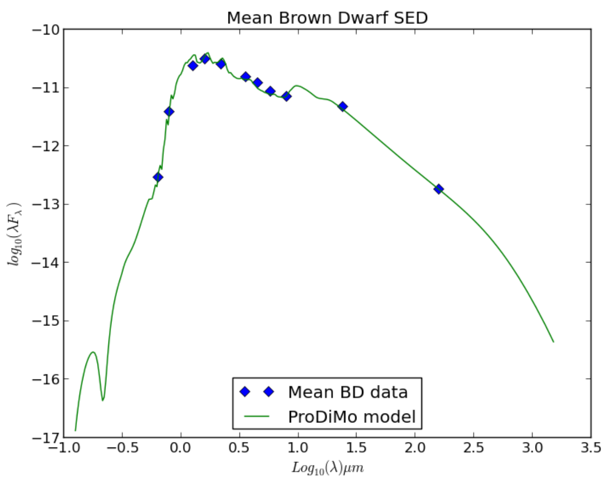

(c)

Figure 1: *ProDiMo results. top: The HCO+ distribution in mean brown dwarf model (a) and T Tauri model (b) with overplotted the dust temperatures and extinction contours. bottom: Mean ProDiMo SED with observed photometric points*

Table 1: *ProDiMo model input parameters*

Model Parameter	Best fitting Brown dwarf model	T Tauri Model
M_*	0.178 $M_\odot$	0.8 $M_\odot$
L_*	0.045 $L_\odot$	0.7 $L_\odot$
T_{eff}	2700 k	4400 k
M_{disk}	1.68×10^{-4} $M_\odot$	0.01 $M_\odot$
R_{in}	0.0725 AU	0.1 AU
R_{out}	200 AU	300 AU
scale height at 1 AU	0.08 AU	0.1 AU
dust/gas	0.01	0.01
flaring power β	1.03	1.13

References

Alexander, R. D. & Armitage, P. J. 2006, ApJL, 639, L83

Andrews, S. M., Wilner, D. J., Hughes, A. M., Qi, C., Rosenfeld, K. A., Öberg, K. I., Birnstiel, T., Espaillat, C., Cieza, L. A., Williams, J. P., Lin, S.-Y., & Ho, P. T. P. 2012, ApJ, 744, 162

Guieu, S., Pinte, C., Monin, J., François, M., Fukagawa, M., Rebull, L., Padgett, D., Carey, S., McCabe, C., Noriega-Crespo, A., Brooke, T., Huard, T., & Hines, D. 2007, in Bulletin of the American Astronomical Society, Vol. 39, American Astronomical Society Meeting Abstracts, 103.22

Harvey, P. M., Henning, T., Liu, Y., Ménard, F., Pinte, C., Wolf, S., Cieza, L. A., Evans, II, N. J., & Pascucci, I. 2012, ApJ, 755, 67

Hughes, A. M., Wilner, D. J., Qi, C., & Hogerheijde, M. R. 2008, ApJ, 678, 1119

Mohanty, S., Greaves, J., Mortlock, D., Pascucci, I., Scholz, A., Thompson, M., Apai, D., Lodato, G., & Looper, D. 2013, ApJ, 773, 168

Öberg, K. I., Qi, C., Fogel, J. K. J., Bergin, E. A., Andrews, S. M., Espaillat, C., Wilner, D. J., Pascucci, I., & Kastner, J. H. 2011, ApJ, 734, 98

Padoan, P. & Nordlund, Å. 2002, ApJ, 576, 870

Pinilla, P., Birnstiel, T., Benisty, M., Ricci, L., Natta, A., Dullemond, C. P., Dominik, C., & Testi, L. 2013, A&A, 554, A95

Reipurth, B. & Clarke, C. 2001, AJ, 122, 432

Ricci, L., Testi, L., Natta, A., Scholz, A., & de Gregorio-Monsalvo, I. 2012, ApJL, 761, L20

Ricci, L., Testi, L., Natta, A., Scholz, A., de Gregorio-Monsalvo, I., Isella, A., & Carpenter, J. M. 2013, ArXiv e-prints

Woitke, P., Kamp, I., & Thi, W.-F. 2009, A&A, 501, 383

ID Not Assigned

SG : 1 of 2 Measurement of extent of gas in the disl Band 6

In the first science goal we measure the radial extent of gas in the disk. Various models predict the values to be close to 200AU. This measurement will throw some light on the formation process of the disk and also explain the optical thickness of the disk which affects the disk chemistry.

Science Goal Parameters

Ang.Res.	LAS	RMS	RMS Bandwidth	Rep.Freq.	Cont. RMS	Cont. Bandwidth	Poln.Prod.
0.18"	0.0"	10 mJy, 7.1 K	122.070 kHz	230.538000 GHz	228.22 µJy, 162 mK	0.234 GHz	XX,YY

Use of 12m Array (34 antennas)

t_total (all configs)	t_science (extended)	t_total(compact)	Imaged area	#12m pointing	12m Mosaic spacing	HPBW	t_per_point	Data Vol	Data Rate
4.8 h	2.3 h	0.0 s	8.9 "	11	offset	26.8 "	774.2 s	92.2 GB	5.4 MB/s

Use of ACA 7m Array (9 antennas) and TP Array

t_total(ACA)	t_total(7m)	t_total(TP)	Imaged area	#7m pointing	7m Mosaic spacing	HPBW	t_per_point	Data Vol	Data Rate

11 Targets

No.	Target	Ra,Dec(J2000)	V,def,frame --OR--z
1	1-CHFT-Tau_9	04:24:26, 26:49:50	0.0 km/s,lsrk,OPTICAL
2	2-KPNO-Tau_6	04:30:07, 26:08:20	0.0 km/s,lsrk,OPTICAL
3	3-KPNO-Tau_7	04:30:57, 25:56:39	0.0 km/s,lsrk,OPTICAL
4	4-CHFT-Tau_12	04:33:09, 22:46:48	0.0 km/s,lsrk,OPTICAL
5	5-BDD_399	04:38:14, 26:11:39	0.0 km/s,lsrk,OPTICAL
6	6-GM_Tau	04:38:21, 26:09:13	0.0 km/s,lsrk,OPTICAL
7	7-CHFT-Tau_6	04:39:03, 25:44:24	0.0 km/s,lsrk,OPTICAL
8	8-CHFT-Tau_4	04:39:47, 26:01:40	0.0 km/s,lsrk,OPTICAL
9	9-CHFT-Tau_8	04:41:10, 25:55:11	0.0 km/s,lsrk,OPTICAL
10	10-BDD_304	04:41:48, 25:34:30	0.0 km/s,lsrk,OPTICAL
11	11-BDD_164	04:44:27, 25:12:16	0.0 km/s,lsrk,OPTICAL

Expected Source Properties

	Peak Flux	SNR	Pol.	Pol. SNR	Linewidth
Line	30.00 mJy	3.0	0%	0.0	1 km/s
Continuum	0.35 mJy	1.5	0%	0.0	0 km/s

Dynamic range (cont flux/line rms): 0.0

1 Tuning

Tuning	Target	Rep. Freq. Sky GHz	RMS (Rep. Freq.)	RMS Achieved
1	1,2,3,4,5,...	230.538000	10 mJy, 7.1 K	10 - 10 mJy

Spectral Setup : Spectral Line

BB	Center Freq Rest GHz	Line ID	Eff #Ch p.p.	Bandwidth	Resolution	Vel. Bandwidth	Vel. Res.	Res. El. per FWHM
1	230.538000	CO v=0 2-1	3840	234.4 MHz	122.07 kHz	305 km/s	0.2 km/s	5

ID Not Assigned

SG : 2 of 2 Detection of Photochemistry in the dis Band 7

In this science goal we detect gas phase emissions around cold regions of the disk, where the photochemistry dominates in the disk.

Science Goal Parameters

Ang.Res.	LAS	RMS	RMS Bandwidth	Rep.Freq.	Cont. RMS	Cont. Bandwidth	Poln.Prod.
0.50"	0.0"	10 mJy, 384.3 mK	244.141 kHz	356.734242 GHz	228.22 µJy, 8.8 mK	0.469 GHz	XX,YY

Use of 12m Array (34 antennas)

t_total (all configs)	t_science (extended)	t_total(compact)	Imaged area	#12m pointing	12m Mosaic spacing	HPBW	t_per_point	Data Vol	Data Rate
2.6 h	1.1 h	0.0 s	5.8 "	3	offset	17.3 "	1306.4 s	49.0 GB	5.4 MB/s

Use of ACA 7m Array (9 antennas) and TP Array

t_total(ACA)	t_total(7m)	t_total(TP)	Imaged area	#7m pointing	7m Mosaic spacing	HPBW	t_per_point	Data Vol	Data Rate

3 Targets

No.	Target	Ra,Dec(J2000)	V,def,frame --OR--z
1	1-CHFT-Tau_6	04:39:03, 25:44:24	0.0 km/s,lsrk,OPTICAL
2	2-CHFT-Tau_4	04:39:47, 26:01:40	0.0 km/s,lsrk,OPTICAL
3	3-2MASS_0444+25...	04:44:27, 25:12:16	0.0 km/s,lsrk,OPTICAL

Expected Source Properties

	Peak Flux	SNR	Pol.	Pol. SNR	Linewidth
Line	50.00 mJy	5.0	0%	0.0	1 km/s
Continuum	1.00 mJy	4.4	0%	0.0	0 km/s

Dynamic range (cont flux/line rms): 0.1

1 Tuning

Tuning	Target	Rep. Freq. Sky GHz	RMS (Rep. Freq.)	RMS Achieved
1	1,2,3	356.734242	10 mJy, 384.3 mK	10 - 10 mJy

Spectral Setup : Spectral Line

BB	Center Freq Rest GHz	Line ID	Eff #Ch p.p.	Bandwidth	Resolution	Vel. Bandwidth	Vel. Res.	Res. El. per FWHM
1	356.734242	HCO+ v=0 4-3	3840	468.8 MHz	244.14 kHz	394 km/s	0.2 km/s	3

BIBLIOGRAPHY

Alexander, R. D., & Armitage, P. J. 2006, ApJL, 639, L83

Andre, P., Ward-Thompson, D., & Barsony, M. 1993, ApJ, 406, 122

Andrews, S. M., & Williams, J. P. 2007, ApJ, 659, 705

Andrews, S. M., Wilner, D. J., Hughes, A. M., et al. 2012, ApJ, 744, 162

Apai, D., Pascucci, I., Sterzik, M. F., et al. 2004, A&A, 426, L53

Armitage, P. 2010, Astrophysics of Planet Formation (Cambridge University Press)

Auer, L. H. 1984, Difference equations and linearization methods for radiative transfer, ed. W. Kalkofen, 237–279

Basri, G., Marcy, G. W., & Graham, J. R. 1996, ApJ, 458, 600

Bate, M. R. 2012, MNRAS, 419, 3115

Bate, M. R., Bonnell, I. A., & Bromm, V. 2002, MNRAS, 336, 705

Bonnell, I. A., Clark, P., & Bate, M. R. 2008, MNRAS, 389, 1556

Chiang, E. I., & Goldreich, P. 1997, ApJ, 490, 368

de Laplace, P. 1809, The System of the World, The System of the World No. v. 2 (Richard Phillips)

Draine, B. T. 1978, ApJS, 36, 595

Draine, B. T., & Bertoldi, F. 1996, ApJ, 468, 269

Dullemond, C. P., Hollenbach, D., Kamp, I., & D'Alessio, P. 2007, Protostars and Planets V, 555

Greene, T. P., Wilking, B. A., Andre, P., Young, E. T., & Lada, C. J. 1994, ApJ, 434, 614

Guieu, S., Pinte, C., Monin, J.-L., et al. 2007, A&A, 465, 855

Harvey, P. M., Henning, T., Ménard, F., et al. 2012, ApJL, 744, L1

Hayashi, C., & Nakano, T. 1963, Progress of Theoretical Physics, 30, 460

Hogerheijde, M. R., & van der Tak, F. F. S. 2000, A&A, 362, 697

Hughes, A. M., Wilner, D. J., Qi, C., & Hogerheijde, M. R. 2008, ApJ, 678, 1119

Kamp, I., Tilling, I., Woitke, P., Thi, W.-F., & Hogerheijde, M. 2010, A&A, 510, A18

Kamp, I., Woitke, P., Pinte, C., et al. 2011, A&A, 532, A85

Kant, I. 1969, Universal Natural History and Theory of the Heavens, Ann Arbor paperbacks (University of Michigan Press)

Kumar, S. S. 1963, ApJ, 137, 1121

Lada, C. J., & Wilking, B. A. 1984, ApJ, 287, 610

Luhman, K. L. 1999, ApJ, 525, 466

—. 2012, ARAA, 50, 65

Luhman, K. L., Adame, L., D'Alessio, P., et al. 2005, ApJL, 635, L93

Mathews, G. S., Pinte, C., Duchêne, G., Williams, J. P., & Ménard, F. 2013, A&A, 558, A66

Mayne, N. J., Harries, T. J., Rowe, J., & Acreman, D. M. 2012, MNRAS, 423, 1775

McMullin, J., Waters, B., Schiebel, D., Young, W., & Golap, K. 2007, RA Shaw, F. Hill, & DJ Bell (San Francisco, CA: ASP), 127

Mohanty, S., Greaves, J., Mortlock, D., et al. 2013, ApJ, 773, 168

Muench, A. A., Alves, J., Lada, C. J., & Lada, E. A. 2001, ApJL, 558, L51

Mulders, G. D., & Dominik, C. 2012, A&A, 539, A9

Nakajima, T., Oppenheimer, B. R., Kulkarni, S. R., et al. 1995, Nature, 378, 463

Oppenheimer, B. R., Kulkarni, S. R., Matthews, K., & Nakajima, T. 1995, Science, 270, 1478

Padoan, P., & Nordlund, Å. 2002, ApJ, 576, 870

Pinilla, P., Birnstiel, T., Benisty, M., et al. 2013, A&A, 554, A95

Rebolo, R., Zapatero Osorio, M. R., & Martín, E. L. 1995, Nature, 377, 129

Reipurth, B., & Clarke, C. 2001, AJ, 122, 432

Ricci, L., Testi, L., Natta, A., Scholz, A., & de Gregorio-Monsalvo, I. 2012, ApJL, 761, L20

Ricci, L., Testi, L., Natta, A., et al. 2014, ArXiv e-prints, arXiv:1406.0635

Röllig, M., Abel, N. P., Bell, T., et al. 2007, A&A, 467, 187

Siess, L., Dufour, E., & Forestini, M. 2000, A&A, 358, 593

Stahler, S., & Palla, F. 2008, The Formation of Stars (Wiley)

Stamatellos, D., & Whitworth, A. P. 2009, MNRAS, 392, 413

Ter Haar, D. 1967, ARAA, 5, 267

Tognelli, E., Prada Moroni, P. G., & Degl'Innocenti, S. 2011, A&A, 533, A109

van Dishoeck, E. F., Jonkheid, B., & van Hemert, M. C. 2008, ArXiv e-prints, arXiv:0806.0088

Whitworth, A. P., & Goodwin, S. P. 2005, Astronomische Nachrichten, 326, 899

Whitworth, A. P., & Zinnecker, H. 2004, A&A, 427, 299

Williams, J. P., & Cieza, L. A. 2011, ARAA, 49, 67

Woitke, P., Kamp, I., & Thi, W.-F. 2009, A&A, 501, 383

Woitke, P., Pinte, C., Tilling, I., et al. 2010, MNRAS, 405, L26

Woodall, J., Agúndez, M., Markwick-Kemper, A. J., & Millar, T. J. 2007, A&A, 466, 1197